

# Bioresorbable silicon electronic sensors for the brain

Seung-Kyun Kang<sup>1,2\*</sup>, Rory K. J. Murphy<sup>3\*</sup>, Suk-Won Hwang<sup>4\*</sup>, Seung Min Lee<sup>1,2\*</sup>, Daniel V. Harburg<sup>1,2</sup>, Neil A. Krueger<sup>1</sup>, Jiho Shin<sup>2,5</sup>, Paul Gamble<sup>3</sup>, Huanyu Cheng<sup>6</sup>, Sooyoun Yu<sup>2,5</sup>, Zhuangjian Liu<sup>7</sup>, Jordan G. McCall<sup>8</sup>, Manu Stephen<sup>3</sup>, Hanze Ying<sup>1</sup>, Jeonghyun Kim<sup>1,2</sup>, Gayoung Park<sup>9,10</sup>, R. Chad Webb<sup>1,2</sup>, Chi Hwan Lee<sup>11</sup>, Sangjin Chung<sup>1,2</sup>, Dae Seung Wie<sup>12</sup>, Amit D. Gujar<sup>3</sup>, Bharat Vemulapalli<sup>3</sup>, Albert H. Kim<sup>3</sup>, Kyung-Mi Lee<sup>10</sup>, Jianjun Cheng<sup>1</sup>, Younggang Huang<sup>13</sup>, Sang Hoon Lee<sup>14</sup>, Paul V. Braun<sup>1,2,15</sup>, Wilson Z. Ray<sup>3</sup> & John A. Rogers<sup>1,2,15</sup>

Many procedures in modern clinical medicine rely on the use of electronic implants in treating conditions that range from acute coronary events to traumatic injury<sup>1,2</sup>. However, standard permanent electronic hardware acts as a nidus for infection: bacteria form biofilms along percutaneous wires, or seed haematogenously, with the potential to migrate within the body and to provoke immune-mediated pathological tissue reactions<sup>3,4</sup>. The associated surgical retrieval procedures, meanwhile, subject patients to the distress associated with re-operation and expose them to additional complications<sup>5–8</sup>. Here, we report materials, device architectures, integration strategies, and *in vivo* demonstrations in rats of implantable, multifunctional silicon sensors for the brain, for which all of the constituent materials naturally resorb via hydrolysis and/or metabolic action<sup>9–12</sup>, eliminating the need for extraction. Continuous monitoring of intracranial pressure and temperature illustrates functionality essential to the treatment of traumatic brain injury<sup>2,13</sup>; the measurement performance of our resorbable devices compares favourably with that of non-resorbable clinical standards. In our experiments, insulated percutaneous wires connect to an externally mounted, miniaturized wireless potentiostat for data transmission. In a separate set-up, we connect a sensor to an implanted (but only partially resorbable) data-communication system, proving the principle that there is no need for any percutaneous wiring. The devices can be adapted to sense fluid flow, motion, pH or thermal characteristics, in formats that are compatible with the body's abdomen and extremities, as well as the deep brain, suggesting that the sensors might meet many needs in clinical medicine.

Figure 1a and Supplementary Fig. 1 show a bioresorbable pressure sensor with a magnified illustration of the active region and its cross-sectional side view. The construction involves a membrane of poly(lactic-co-glycolic acid) (PLGA, with a thickness of 30  $\mu\text{m}$ ), sealed against a supporting substrate of nanoporous silicon (60–80  $\mu\text{m}$  thick; 71% porosity) or magnesium foil (60–80  $\mu\text{m}$  thick; see Supplementary Figs 2, 3). The substrate has a square structure of relief (with a depth of 30–40  $\mu\text{m}$ ) etched onto its surface. The associated air cavity allows the membrane to deflect in response to pressure in the fluid surroundings. A silicon nanomembrane in a serpentine geometry serves as a piezoresistive element that rests on the surface

of the membrane near one of the edges of the cavity, where deflection-induced strains are largest (Fig. 1b). The resistance of this sensing element increases monotonically in a linear fashion across the full range of pressures that are relevant to intracranial monitoring (that is, 0–70 mm Hg). An overcoat of silicon oxide ( $\text{SiO}_2$ , about 100 nm thick) provides electrical passivation and a barrier against biofluids. Figure 1c and Supplementary Fig. 4 show photographs of two representative devices of different dimensions to illustrate the scalability of fabrication; the total sizes and weights are 1 mm  $\times$  2 mm  $\times$  0.08 mm (trench size: 0.67 mm  $\times$  0.8 mm  $\times$  0.03 mm) and about 0.4 mg; and 3 mm  $\times$  6 mm  $\times$  0.11 mm (trench size: 2 mm  $\times$  2.4 mm  $\times$  0.04 mm) and roughly 1 mg, respectively.

The mechanics of the system can be captured quantitatively by three-dimensional finite element analysis (FEA). Distributions of principal strains and vertical displacements evaluated at an external pressure of 50 mm Hg appear in Fig. 1d. The maximum strain for any applied pressure over the range of interest occurs at the midpoint of the left (and right) edge of the trench, thus motivating this choice of location for the silicon-nanomembrane piezoresistive element (see Supplementary Methods and Supplementary Figs 5 and 6 for details)<sup>14</sup>. The calibration between pressure and resistance is linear, with a slope of 83  $\Omega(\text{mm Hg})^{-1}$ , consistent with modelling results and a gauge factor of about 30, which lies within a range of expected values for monocrystalline silicon (Supplementary Fig. 7)<sup>15</sup>.

Evaluations in set-ups that resemble the intracranial cavity reveal measured pressure responses that agree quantitatively with those of clinical-standard, non-bioresorbable sensors (Fig. 1e and Supplementary Figs 8–10). With various simple modifications, this same platform can be used for precision measurement of other parameters of interest in biomedicine and clinical care. Examples include: motion sensors built with a cantilevered test mass of PLGA (that is, a single-axis accelerometer, Fig. 1f); temperature sensors that exploit the temperature-dependent resistance of silicon-nanomembrane elements set apart from the cavity structure (Fig. 1g); flow sensors in which the silicon nanomembranes serve simultaneously as heating elements and temperature sensors (Fig. 1h); thermal conductivity/diffusivity sensors that exploit related concepts (Fig. 1i); and pH sensors that rely on electrostatic gating of transport through the silicon nanomembrane (Fig. 1j). In addition, chemically functionalizing the surface of the silicon of this last device provides a route to biomolecular sensing, using

<sup>1</sup>Department of Materials Science and Engineering, University of Illinois at Urbana-Champaign, Urbana, Illinois 61801, USA. <sup>2</sup>Frederick Seitz Materials Research Laboratory, University of Illinois at Urbana-Champaign, Urbana, Illinois 61801, USA. <sup>3</sup>Department of Neurological Surgery, Washington University School of Medicine, St Louis, Missouri 63110, USA. <sup>4</sup>KU-KIST Graduate School of Converging Science and Technology, Korea University, Seoul 136-701, Republic of Korea. <sup>5</sup>Department of Chemical and Biomolecular Engineering, University of Illinois at Urbana-Champaign, Urbana, Illinois 61801, USA. <sup>6</sup>Department of Engineering Science and Mechanics, Materials Research Institute, The Pennsylvania State University, University Park, Pennsylvania 16802, USA. <sup>7</sup>Institute of High Performance Computing, Singapore 138632, Singapore. <sup>8</sup>Department of Anesthesiology, Washington University School of Medicine, St Louis, Missouri 63110, USA. <sup>9</sup>Department of Biomicrosystem Technology, Korea University, Seoul 136-701, South Korea. <sup>10</sup>Department of Biochemistry and Molecular Biology, Korea University College of Medicine, Seoul 136-713, South Korea. <sup>11</sup>Weldon School of Biomedical Engineering, School of Mechanical Engineering, The Center for Implantable Devices, Birck Nanotechnology Center, Purdue University, West Lafayette, Indiana 47907, USA. <sup>12</sup>School of Mechanical Engineering, Purdue University, West Lafayette, Indiana 47907, USA. <sup>13</sup>Department of Mechanical Engineering, Civil and Environmental Engineering, Materials Science and Engineering, and Skin Disease Research Center, Northwestern University, Evanston, Illinois 60208, USA. <sup>14</sup>Department of Biomedical Engineering, College of Health Science, Korea University, Seoul 136-703, South Korea. <sup>15</sup>Beckman Institute for Advanced Science and Technology, University of Illinois at Urbana-Champaign, Urbana, Illinois 61801, USA.

\*These authors contributed equally to this work.

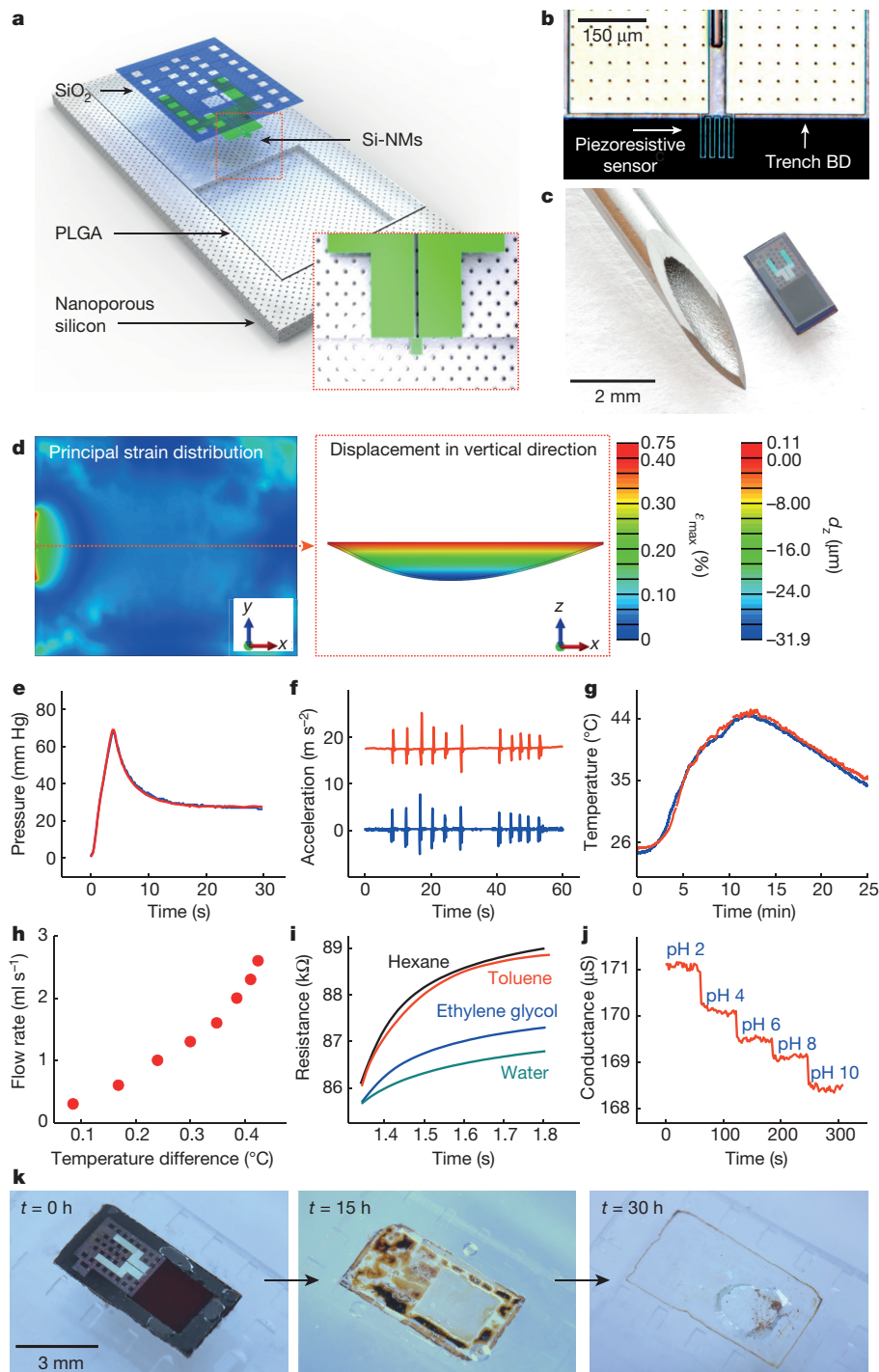


**Figure 1 | Bioresorbable, silicon-based mechanical/physical/chemical sensors for biomedical applications.** **a**, Schematic illustration of a biodegradable pressure sensor. The inset shows the location of the silicon-nanomembrane (Si-NM) strain gauge. **b**, Optical micrograph of the strain-gauge region. ‘Trench BD’, boundary of the trench. **c**, Image of a complete device. The outer diameter of the hypodermic needle is 1 mm. **d**, Left, distribution of principal strains across the PLGA layer, including the Si-NM strain gauge at the left edge, determined from finite element analysis (FEA) for an external pressure of 50 mm Hg. Right, corresponding displacement profile evaluated along the red dotted line in the left panel.  $\varepsilon_{\max}$  and  $d_z$  are the principal strain and vertical displacement, respectively. **e**, Responses of a commercial pressure sensor (blue) and a calibrated biodegradable device (red) to time-varying pressure over a range relevant to intracranial monitoring. **f**, Response of a similar biodegradable device (red), but configured as an accelerometer, with comparison to a commercial sensor (blue). **g**, Comparison of the calibrated response of

such a bioresorbable temperature sensor (red) to a commercial device (blue). **h**, The difference in temperature measured by two separate Si-NM temperature sensors placed near a Si-NM element for Joule heating allows assessment of flow rate. **i**, A single serpentine Si-NM used as both a temperature sensor and a heating element allows measurements of thermal conductivity and heat capacity. The graph shows time-dependent changes in temperature upon actuation of Joule heating in devices immersed in different liquids. The coefficients of thermal conductivity ( $\kappa$ , measured through the rate of resistance change) of hexane, toluene, ethylene glycol, and water are 0.12, 0.13, 0.26, and 0.60  $\text{W m}^{-1} \text{K}^{-1}$ , respectively. **j**, When the Si-NM is exposed to aqueous surroundings, its conductance depends on pH. The graph shows measurements for immersion in solutions with pH values between 2 and 10. **k**, Images collected at several stages of accelerated dissolution of a bioresorbable pressure sensor upon insertion into an aqueous buffer solution (pH 12) in a transparent PDMS enclosure at room temperature.

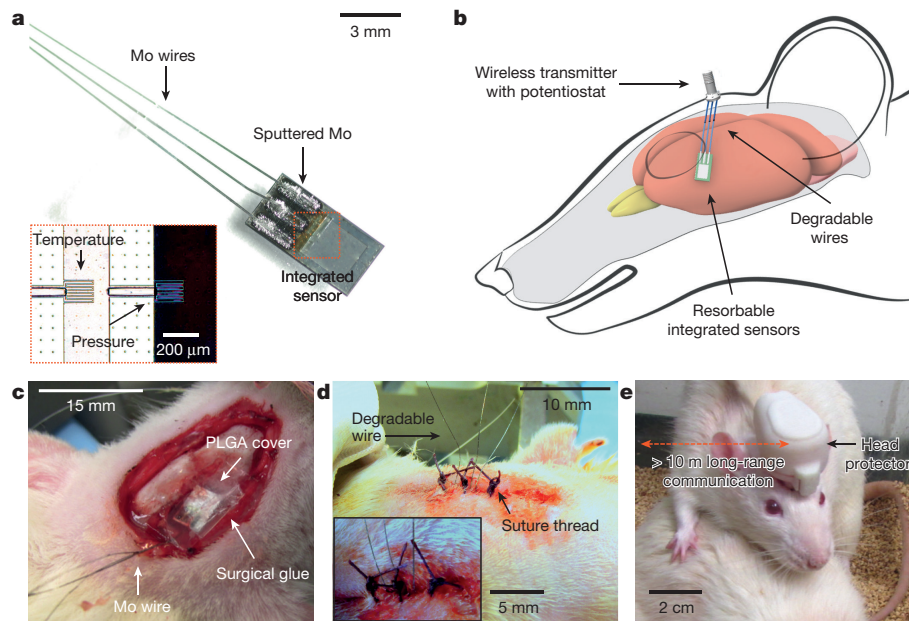


**Figure 2 | Bioresorbable interfaces between intracranial sensors and external wireless data-communication modules with percutaneous wiring.** **a**, Image of bioresorbable pressure and temperature sensors integrated with dissolvable metal interconnects (sputtered molybdenum, Mo, 2  $\mu\text{m}$  thick) and wires (Mo, 10  $\mu\text{m}$  thick). The inset shows an optical micrograph of the serpentine Si-NM structures that form the sensing regions. The Si-NM that is not above the air cavity (left) responds only to temperature; the one at the edge of the air cavity (right) responds primarily

to pressure. **b**, Diagram of a bioresorbable sensor system in the intracranial space of a rat, with electrical interconnects that provide an interface to an external wireless data-transmission unit for long-range operation. **c**, **d**, Demonstrations of **c**, an implanted bioresorbable sensor in a rat, and **d**, a sutured individual. A thin film of PLGA ( $\sim 80 \mu\text{m}$ ) and a degradable surgical glue (TISSEAL) seal the craniectomy defect to close the intracranial cavity. **e**, Healthy, freely moving rat equipped with a complete, biodegradable wireless intracranial sensor system.

schemes similar to those in conventional silicon biosensors<sup>16–18</sup>. The fabrication methods and operating principles for each of the modalities in Fig. 1f–j appear in Supplementary Methods and Supplementary Figs 11–15.

The uniqueness of these devices is their ability to dissolve completely into biocompatible end products when immersed in aqueous solutions, including biofluids such as cerebrospinal fluid (CSF). Hydrolysis of the silicon nanomembranes, the layers of  $\text{SiO}_2$ , the thin wafers of nanoporous silicon and the magnesium foils causes loss of material at rates of 23  $\text{nm day}^{-1}$ , 8  $\text{nm day}^{-1}$ , 9  $\mu\text{m day}^{-1}$  and 4  $\mu\text{m day}^{-1}$ , respectively, in artificial CSF (ACSF) at physiological temperature (37  $^{\circ}\text{C}$ ) (Supplementary Fig. 16). Separate studies indicate that PLGA (75:25 (lactide:glycolide) composition) dissolves in biofluids within four to five weeks<sup>19</sup>. To illustrate the various stages of dissolution of a completed system, Fig. 1k shows a sequence of images of a bioresorbable pressure sensor inserted into a transparent chamber designed for accelerated testing (polydimethylsiloxane (PDMS) enclosure filled with buffer solution at pH 12 and room temperature), in which fluid exchange can occur through an array of openings around the perimeter (Supplementary Fig. 17). Supplementary Fig. 18 presents images of nanoporous silicon and silicon nanomembranes observed by scanning electron microscopy at different times during hydrolysis. The silicon nanomembrane dissolves uniformly, without fracture. By comparison, nanoporous silicon dissolves less uniformly, with a tendency to form fragments. Here, the silicon-nanomembrane and  $\text{SiO}_2$  components dissolve first, within 15 hours, followed by the nanoporous silicon, which disappears within 30 hours. In all cases, the dissolution kinetics depends strongly on the materials and the composition of the surrounding solution<sup>20–22</sup>. Supplementary Table 1 summarizes the hydrolysis mechanisms and dissolution rates of these materials in a representative solution. As described below, the encapsulation material and its thickness define the operational lifetimes.

Figure 2 illustrates a strategy for using these types of bioresorbable systems for wireless pressure and temperature monitoring in the intracranial space of rats. Figure 2a shows a photograph of a device

like the one in Fig. 1c, but configured to allow simultaneous sensing of both pressure and temperature. The measured temperature can also be used to calibrate against parasitic effects of this parameter on the pressure determination (see Supplementary Methods and Supplementary Fig. 19). Biodegradable molybdenum wires (10  $\mu\text{m}$  thick) serve as an interface to wireless communication systems. Pressing the interconnect wires (molybdenum, 10  $\mu\text{m}$  thick, or magnesium, 50  $\mu\text{m}$  thick) against the PLGA at elevated temperatures (65  $^{\circ}\text{C}$ ) embeds them near the surface but leaves the top regions exposed, thereby allowing for deposition of biodegradable metals (molybdenum, 2  $\mu\text{m}$  thick) to form electrical contact pads through stencil masks (made from the polyimide Kapton, 12.5  $\mu\text{m}$  thick; Supplementary Fig. 20). The deposited molybdenum forms stable interconnects between metal wires and silicon nanomembranes that are fully embedded on PLGA. Encapsulation with a bioresorbable polymer (polyanhydride, discussed in more detail below) enhances system robustness by reducing the stress concentrations at the interconnections. Narrow strips of PLGA laminated onto the front and back sides of the wires along their entire lengths act as electrical insulation. These insulated wires connect to an externally mounted, miniaturized wireless potentiostat for transmission of data thorough percutaneous wiring. Figure 2b provides a diagram of such a system in the intracranial space of a rat model. The sensor subsystem connects via molybdenum wires to the wireless module, which is mounted on the top of the skull. Figure 2c–e summarizes the surgical process. A PLGA sheet (about 80  $\mu\text{m}$  thick) and a dissolvable surgical glue (Fig. 2c) seal the craniectomy defect to close the intracranial cavity. Conventional sutures hold the surgical site closed, in a standard process<sup>23</sup> that retains points at which the dissolvable wires emerge from the skin to allow electrical connection (Fig. 2d). These wires have dimensions comparable to those of the surgical threads, and therefore pose little additional risk. Figure 2e shows a healthy, freely moving rat with a complete system. Supplementary Fig. 21 presents images of the connections.

Figure 3 summarizes the results of a comprehensive set of wireless measurements of intracranial pressure (ICP) and intracranial

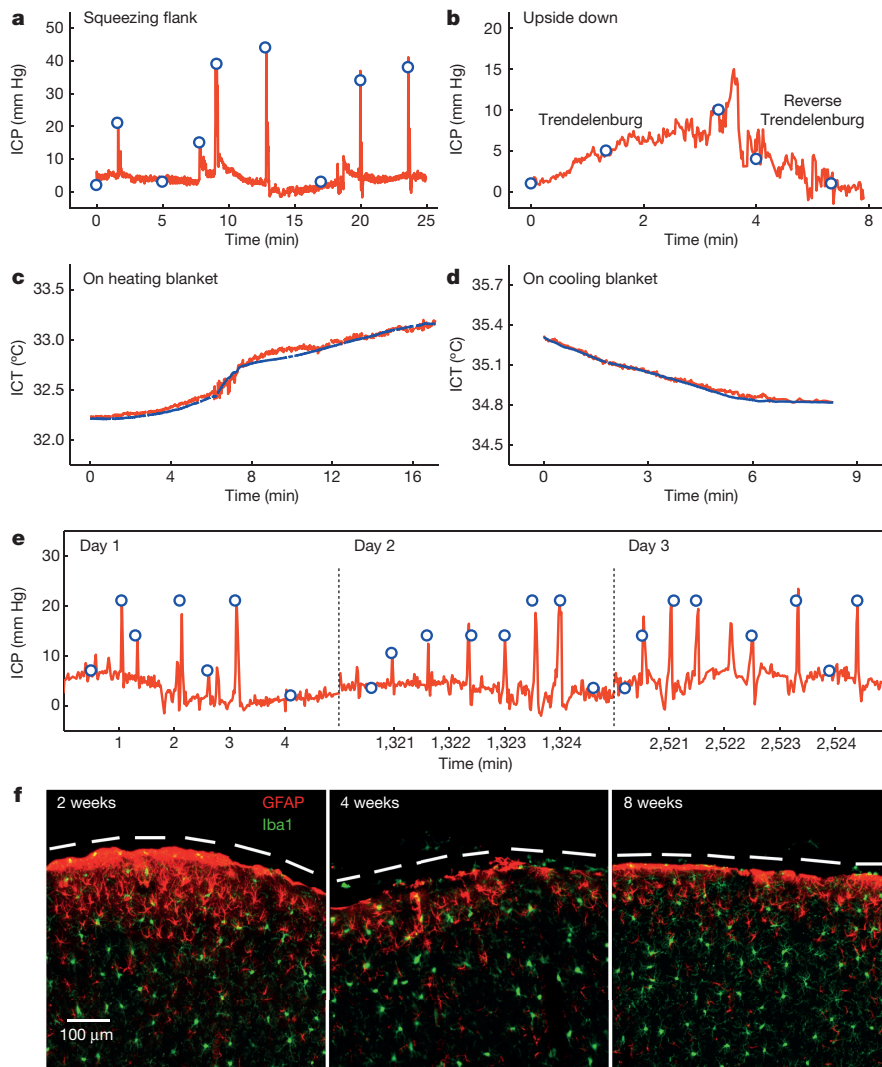


**Figure 3 | Wireless measurement of intracranial pressure and temperature with bioresorbable sensors implanted in live, freely moving animals.** **a–e**, Red, data from a transient, bioresorbable sensor; blue, data from a commercial sensor. **a**, Real-time wireless measurements of ICP, showing transient increases induced by the Valsalva manoeuvre. **b**, *In vivo* observation of changes in ICP as a function of time in the Trendelenburg and reverse Trendelenburg positions. ICP increases in the 30° head-down position (Trendelenburg) as compared with the supine position, and decreases in the 30° head-up position (reverse Trendelenburg). **c**, Gradual increase and **d**, decrease in ICT due to

temperature (ICT), recorded in rats with percutaneous wired systems. The ICP traces reveal features that correspond to periodic manual abdominal compression activating the Valsalva manoeuvre, which yields rapid increases or decreases in ICP (Fig. 3a)<sup>24</sup>. Gentle changes in the rat's position—that is, Trendelenburg (30° head-down position) and reverse Trendelenburg (30° head-up position)—produce gradual increases and decreases in ICP, respectively (Fig. 3b), as would be expected because of the corresponding accumulation and depletion of blood in the brain<sup>25</sup>. The pressure values compare well with those determined using a clinical-standard, wired ICP sensor implanted in the same region of the same animal. The wireless, bioresorbable ICT sensors perform to levels of accuracy similar to those of commercial sensors: Fig. 3c and d show comparative data collected by modulating the cranial temperature with a heating or cooling blanket placed beneath the animal.

The operational lifetimes of the devices are defined by dissolution of the encapsulation layers and the permeation of fluids through them. *In vitro* experiments using a bioresorbable pressure sensor

application of a heating/cooling blanket. **e**, Measurements of ICP over three days reveal consistent responses from devices encapsulated with biodegradable polyanhydride. **f**, Confocal fluorescence images of the cortical surface beneath the dissolved device at 2, 4 and 8 weeks, showing the absence of inflammatory responses. The images are double-immunostained for GFAP (glial fibrillary acidic protein) to detect astrocytes (red), and Iba1 (ionized calcium-binding adaptor molecule 1) to identify microglia/macrophages (green). The dashed line indicates the site of the implant.

encapsulated with a film of a specially synthesized polyanhydride (about 120 μm thick; Supplementary Fig. 22) show expected performance and accurate readings with an appropriately modified calibration factor ( $50 \Omega(\text{mm Hg})^{-1}$ ). The slow dissolution rate of the polyanhydride (about  $1.3 \mu\text{m day}^{-1}$ )—together with the modest change in sensitivity that occurs depending on the thickness of this material (about  $0.34 \Omega(\text{mm Hg})^{-1} \mu\text{m}^{-1}$ )—leads to a loss of accuracy of only a few per cent when operated over several days. This error falls within standards defined by the Association for the Advancement of Medical Instrumentation (AAMI) for pressure monitoring, that is,  $\pm 2 \text{ mm Hg}$  (from 0 to 20 mm Hg) and  $\pm 10\%$  (from 20 to 100 mm Hg)<sup>2</sup>. (Supplementary Methods and Supplementary Figs 23–25 present information on the synthesis/hydrolysis chemistry, dissolution kinetics, water permeability, and biocompatibility of the polyanhydride.)

Stable, continuous operation is possible for up to three days (Supplementary Fig. 26). Beyond this period, water tends to pass through the polyanhydride and PLGA into the electrically active regions of the device and the air cavity. The resistance remains

relatively constant for seven days, and then begins to increase markedly, mainly because of dissolution of the molybdenum wires and interconnection metal (Supplementary Figs 27 and 28). Figure 3e illustrates *in vivo* operation for three days without notable degradation in absolute accuracy or sensitivity, as benchmarked against a standard, non-resorbable wired sensor. Supplementary Fig. 29 shows similar data from the temperature sensor, where the absence of an air cavity affords enhanced stability, and accurate measurements for six days of operation. These timeframes are relevant for clinical use: ICP and ICT are typically monitored continuously for several days after traumatic brain injury. The chemistry, thickness and composition of the encapsulating layers can be selected to extend the functional lifetimes<sup>26</sup>.

Biocompatibility of the devices through all stages of their life cycle is essential. Comprehensive studies of the immunohistochemistry of brain tissues at several times after implantation (two, four and eight weeks) demonstrate that the sensors and the by-products of their dissolution in the intracranial space are biocompatible. Representative confocal fluorescence images (see Fig. 3f for nanoporous silicon and Supplementary Fig. 30 for magnesium foil) indicate no overt reaction of brain glial cells to the sensor, and no focal aggregation of glial cells at the implantation site for all time ranges. Astrocytosis (an increase in the number of astrocyte cells) and microglial activity at the cortical surface are within normal limits, indicating no overt immune reaction to the device and its by-products. Although the percutaneous wiring does not noticeably affect animal behaviour (see Supplementary Methods and Supplementary Fig. 31), a miniaturized, fully implantable wireless communication system might offer advantages, by removing the possibility of secondary infection at the wires. A wireless system constructed mostly, but not entirely, of resorbable materials (~85% by mass and ~86% by volume)—using an advanced near-field communication-technology approach, with fully bioresorbable metal coils, substrates and encapsulation layers—appears in Extended Data Fig. 1, Methods, and Supplementary Figs 32–37.

Given that these devices function successfully in the intracranial space, they could also be used in other organs and body compartments. As an example, Fig. 4a and b illustrate ICP monitoring using the same bioresorbable device in modes with relevance to acute abdominal compartment syndrome and acute compartment syndrome of the extremity<sup>27,28</sup>. Furthermore, modifying the devices to allow them to be injected deep into tissues could address other needs in clinical treatment. For example, monitoring physiological parameters of the deep brain with intraparenchymal sensors could yield data that are unavailable from the surface or the intracranial space. In addition, because electrophysiological and metabolic abnormalities often emanate from infarcts, contusions and haematomas that damage adjacent intact tissue, sensors of pressure, temperature, pH and other physical/chemical parameters that are placed into the parenchyma within the blood-deprived (ischaemic) penumbra could advance our knowledge of secondary brain injury<sup>29–31</sup>. Such considerations apply not only to injured brain tissue, but also to acute or chronic ischaemia that threatens the heart, limbs, intra-abdominal organs or grafts.

Modifying the geometry of the supporting structures introduced in Fig. 1 enables delivery of bioresorbable sensors into the depths of brain tissue, for direct measurements of injury or status. Figure 4c shows an example that integrates a bioresorbable ICP sensor onto a magnesium foil, formed with a tip region that allows injection into tissues of interest (Supplementary Fig. 38). Mounting the device on a stereotactic frame and fixture allows accurate positioning and controlled penetration (Supplementary Fig. 39). Figure 4d and e summarize pressure and temperature data collected at a site about 5 mm beneath the surface of the rat brain. The Valsalva manoeuvre yields data that quantitatively agree with those obtained using conventional sensors at a similar location. The device detected changes in temperature during anaesthesia (the temperature decreased, owing to reduced blood circulation) and waking up (the temperature returned to normal), as expected of intraparenchymal tissue.

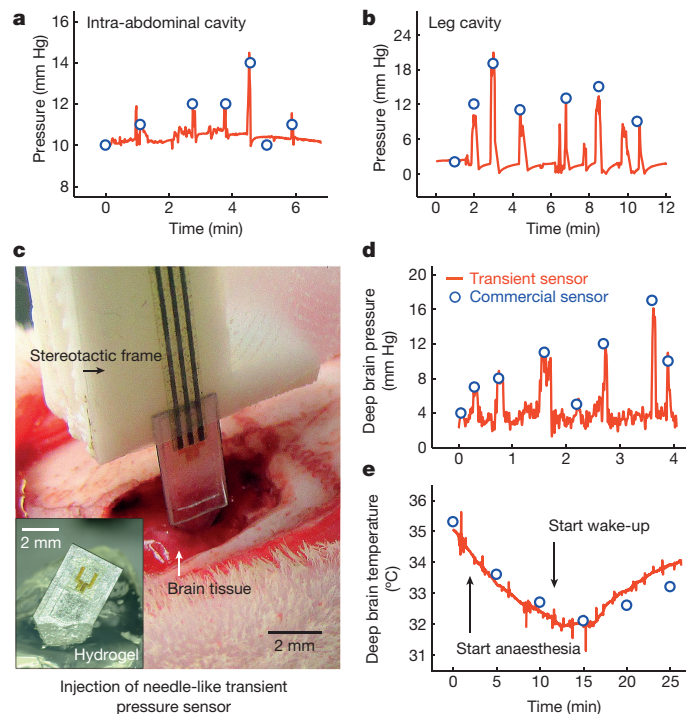


**Figure 4 | Application of bioresorbable sensors to various body cavities, and demonstration of an injectable format for deep brain monitoring.** Red, data from a transient biodegradable sensor; blue, data from a commercial sensor. **a, b**, Pressures measured in **a**, intra-abdominal and **b**, leg cavities. **c**, Image showing *in vivo* injection of a needle-shaped biodegradable pressure sensor (using a magnesium foil support, ~80  $\mu\text{m}$  thick) into the brain parenchyma with a stereotactic frame and arm. The inset shows a biodegradable pressure sensor inserted into hydrogel, as evidence of the sensor's robust mechanical construction. **d**, *In vivo* measurements of pressure in the deep brain. **e**, *In vivo* measurements of temperature in the deep brain during anaesthesia. The temperature drops during anaesthesia owing to reduced blood circulation, and returns to normal after awakening.

The biomedical sensors reported here enable wireless data collection in body cavities and in deep tissues, with platforms that are fully bioresorbable, thereby allowing patients to be monitored until homeostasis has been achieved, and avoiding the risks associated with chronically implanted devices or their removal<sup>32,33</sup>. *In vivo* and *in vitro* experiments demonstrate precision measurements of pressure, temperature, motion, flow, thermal properties and pH, with possible extensions to biomolecular binding events. These features will be useful in diagnosing and treating a diverse range of medical conditions, from acute traumatic injuries such as extremity compartment syndrome, to chronic medical diseases such as diabetes. The materials, manufacturing methods and design layouts should be relevant to many other sensor modalities, with the potential for co-integration of advanced silicon-based integrated circuits, radio communication technologies, power supply and energy harvesters—each adapted from advances in transient electronics. Thus, it is realistic to expect that these devices could be used in sensing, recording, stimulating, and electrical control for medical monitoring and treatment, not only for the body regions explored here but also for areas such as the cardiac space and spinal system. Translating these technologies into clinical settings should provide patients and medical professionals with a vital set of tools for combating human disease.

**Online Content** Methods, along with any additional Extended Data display items and Source Data, are available in the online version of the paper; references unique to these sections appear only in the online paper.

Received 14 March; accepted 18 November 2015.

Published online 18 January 2016.

- Poole, J. E. Present guidelines for device implantation: clinical considerations and clinical challenges from pacing, implantable cardiac defibrillator, and cardiac resynchronization therapy. *Circulation* **129**, 383–394 (2014).
- Brain, T. F. Guidelines for the management of severe traumatic brain injury. VI. Indications for intracranial pressure monitoring. *J. Neurotrauma* **24**, S37–S44 (2007).
- Chamis, A. L. *et al.* Staphylococcus aureus bacteremia in patients with permanent pacemakers or implantable cardioverter-defibrillators. *Circulation* **104**, 1029–1033 (2001).
- Hall-Stoodley, L., Costerton, J. W. & Stoodley, P. Bacterial biofilms: from the natural environment to infectious diseases. *Nature Rev. Microbiol.* **2**, 95–108 (2004).
- Maytin, M. & Epstein, L. M. Lead extraction is preferred for lead revisions and system upgrades. *Circ. Arrhythm. Electrophysiol.* **3**, 413–424 (2010).
- Boutry, C. M. *et al.* Towards biodegradable wireless implants. *Phil. Trans. R. Soc. A* **370**, 2418–2432 (2012).
- Ott, K. *et al.* Retained intracranial metallic foreign bodies: report of two cases. *J. Neurosurg.* **44**, 80–83 (1976).
- Vajramani, G. V. *et al.* Persistent and intractable ventriculitis due to retained ventricular catheters. *Br. J. Neurosurg.* **19**, 496–501 (2005).
- Hwang, S.-W. *et al.* A physically transient form of silicon electronics. *Science* **337**, 1640–1644 (2012).
- Irimia-Vladu, M. “Green” electronics: biodegradable and biocompatible materials and devices for sustainable future. *Chem. Soc. Rev.* **43**, 588–610 (2014).
- Bettinger, C. J. & Bao, Z. Organic thin film transistors fabricated on resorbable biomaterial substrates. *Adv. Mater.* **22**, 651–655 (2010).
- Luo, M., Martinez, A. W., Song, C., Herrault, F. & Allen, M. G. A microfabricated wireless RF pressure sensor made completely of biodegradable materials. *J. Microelectromech. Syst.* **23**, 4–13 (2014).
- Brogan, M. E. & Manno, E. M. Treatment of malignant brain edema and increased intracranial pressure after stroke. *Curr. Treat. Options Neurol.* **17**, 327 (2015).
- Liu, C. *Foundations of MEMS* Ch. 6 (Prentice Hall, 2011).
- Moseley, P. T. & Crocker, J. *Sensor Materials* Ch. 4 (Institute of Physics Publishing, 1994).
- Chang, H. *et al.* DNA-mediated fluctuations in ionic current through silicon oxide nanopore channels. *Nano Lett.* **4**, 1551–1556 (2004).
- Zheng, G., Patolsky, F., Cui, Y., Wang, W. U. & Lieber, C. M. Multiplexed electrical detection of cancer markers with nanowire sensor arrays. *Nature Biotechnol.* **23**, 1294–1301 (2005).
- Stern, E. *et al.* Label-free immunodetection with CMOS-compatible semiconducting nanowires. *Nature* **445**, 519–522 (2007).
- Gentile, P., Chiono, V., Carmagnola, I. & Hatton, P. V. An overview of poly(lactic-co-glycolic) acid (PLGA)-based biomaterials for bone tissue engineering. *Int. J. Mol. Sci.* **15**, 3640–3659 (2014).
- Hwang, S.-W. *et al.* Dissolution chemistry and biocompatibility of single-crystalline silicon nanomembranes and associated materials for transient electronics. *ACS Nano* **8**, 5843–5851 (2014).
- Kang, S.-K. *et al.* Dissolution behaviors and applications of silicon oxides and nitrides in transient electronics. *Adv. Funct. Mater.* **24**, 4427–4434 (2014).
- Yin, L. *et al.* Dissolvable metals for transient electronics. *Adv. Funct. Mater.* **24**, 645–658 (2014).
- Uslaner, J. M. *et al.* T-type calcium channel antagonism produces antipsychotic-like effects and reduces stimulant-induced glutamate release in the nucleus accumbens of rats. *Neuropharmacol.* **62**, 1413–1421 (2012).
- Barth, K. N. M., Onesti, S. T., Krauss, W. E. & Solomon, R. A. A simple and reliable technique to monitor intracranial pressure in the rat: technical note. *Neurosurgery* **30**, 138–140 (1992).
- Haure, P., Cold, G. E., Hansen, T. M. & Larsen, J. R. The ICP-lowering effect of 10° reverse Trendelenburg position during craniotomy is stable during a 10-minute period. *J. Neurosurg. Anesthesiol.* **15**, 297–301 (2003).
- Morgan, P. W. Structure and moisture permeability of film-forming polymers. *Ind. Eng. Chem.* **45**, 2296–2306 (1953).
- Meldrum, D. R. *et al.* Prospective characterization and selective management of the abdominal compartment syndrome. *Am. J. Surg.* **174**, 667–673 (1997).
- Olson, S. A. & Glasgow, R. R. Acute compartment syndrome in lower extremity musculoskeletal trauma. *J. Am. Acad. Orthop. Surg.* **13**, 436–444 (2005).
- Stiefel, M. F. *et al.* Reduced mortality rate in patients with severe traumatic brain injury treated with brain tissue oxygen monitoring. *J. Neurosurg.* **103**, 805–811 (2005).
- Timofeev, I. *et al.* Extracellular brain pH with or without hypoxia is a marker of profound metabolic derangement and increased mortality after traumatic brain injury. *J. Cereb. Blood Flow Metab.* **33**, 422–427 (2013).
- Suehiro, E. *et al.* Diverse effects of hypothermia therapy in patients with severe traumatic brain injury based on the computed tomography classification of the traumatic coma data bank. *J. Neurotrauma* **32**, 353–358 (2015).
- Mittal, R. *et al.* Use of bio-resorbable implants for stabilization of distal radius fractures: the United Kingdom patients’ perspective. *Injury* **36**, 333–338 (2005).
- Ye, T. *et al.* Management of grade III open dislocated ankle fractures: combined internal fixation with bioabsorbable screws/rods and external fixation. *J. Am. Podiatr. Med. Assoc.* **101**, 307–315 (2011).

Supplementary Information is available in the online version of the paper.

**Acknowledgements** S.-K.K. and co-workers are funded by the Defense Advanced Research Projects Agency. J.G.M. is supported by the National Institute of Mental Health, grant F31MH101956. The authors thank M. R. Bruchas at Washington University School of Medicine for providing immunohistochemistry facilities; M. R. MacEwan at Washington University School of Medicine for discussions on animal protocols; A. Manocchi at Transient Electronics Inc. for performing the dissolution test of polyanhydride; and H. Ning at Xerion Advanced Battery Corporation for assistance with running the BET measurements. H.C. was a Howard Hughes Medical Institute International Student Research Fellow. S.-W.H. was supported by the Basic Science Research Program through the National Research Foundation of Korea (NRF) funded by the Ministry of Education (grant NRF-2015R1C1A1A02037560). G.P. and K.M.L. were supported by the Basic Science Research Program through the National Research Foundation of Korea (NRF) funded by the Ministry of Science, ICT, and Future Planning (grants NRF-2007-00107 and NRF-2013M3A9D3045719).

**Author Contributions** S.-K.K., S.-W.H., D.V.H., N.A.K., S.Y., J.S., H.Y., R.C.W., C.H.L., S.C., D.S.W., J.C., P.V.B. and J.A.R. designed and fabricated the sensors and interfaces. S.-K.K., S.M.L., J.S., J.K. S.H.L. and J.A.R. designed, fabricated and analysed the near-field communication system with the sensor. S.-K.K., R.K.J.M., S.M.L., D.V.H., H.C., P.G., S.Y., J.S., M.S., R.C.W., C.H.L., B.V., Z.L., Y.H., W.Z.R. and J.A.R. conceived the idea and performed the experiments and analysis. R.K.J.M., P.G., J.G.M., M.S., G.P., A.D.G., A.H.K., K.-M.L. and W.Z.R. analysed the immunohistochemistry. S.-K.K., R.K.J.M., S.-W.H., S.M.L., D.V.H., H.C., W.Z.R. and J.A.R. wrote the manuscript.

**Author Information** Reprints and permissions information is available at [www.nature.com/reprints](http://www.nature.com/reprints). The authors declare no competing financial interests. Readers are welcome to comment on the online version of the paper. Correspondence and requests for materials should be addressed to J.A.R. ([jrogers@illinois.edu](mailto:jrogers@illinois.edu)) or W.Z.R. ([rayz@wudosis.wustl.edu](mailto:rayz@wudosis.wustl.edu)).

## METHODS

**Fabrication of bioresorbable silicon pressure sensors.** Fabrication involved integration of silicon-based, piezoresistive sensing elements onto substrates of PLGA, bonded over cavities etched into the surfaces of nanoporous Si (np-Si) substrates or magnesium foils. Solid-state diffusion of boron yielded highly doped p-type monocrystalline silicon nanomembranes (Si-NMs) on silicon-on-insulator (SOI) wafers (top silicon  $\sim 300$  nm thick, p-type; SOITEC, France). Eliminating the buried oxide with hydrofluoric acid allowed transfer of the Si-NMs onto a bilayer of D-PI (diluted polyimide (poly(pyromellitic dianhydride-co-4,4'-oxydianiline)),  $\sim 200$  nm)/PMMA (poly(methyl methacrylate),  $\sim 300$  nm) on temporary silicon carrier substrates. Photolithography and etching patterned the Si-NMs into structures with serpentine designs. Electron-beam evaporation and spin-casting defined uniform layers of SiO<sub>2</sub> ( $\sim 100$  nm) and D-PI, respectively, to serve the purpose of passivation. Selective dry etching through all of the layers (D-PI/SiO<sub>2</sub>/D-PI/PMMA) formed a mesh structure that enabled release in acetone, for transfer to a film of PLGA ( $\sim 30$   $\mu$ m). Heating these films to temperatures near the glass transition of the PLGA (65 °C) and laminating them onto np-Si substrates (or magnesium foils,  $\sim 60$ – $80$   $\mu$ m) with square regions of etched relief ( $\sim 30$ – $40$   $\mu$ m) formed sealed air cavities upon cooling to room temperature. Additional details appear in Supplementary Information.

**Calibration of the pressure response.** Responses of commercial sensors under environments similar to those in the intracranial cavity allowed absolute pressure calibration for the bioresorbable devices. The experiments involved placing a bioresorbable pressure sensor inside the barrel of a syringe partially filled with ACSF (Ecocyte BioScience, USA) and with a commercial sensor (NeuLog, USA) located at its open end (orifice). Moving the plunger component of the syringe allowed reversible access to well controlled pressures throughout a range relevant to intracranial monitoring (Supplementary Fig. 9). Comparison of the electrical resistance of the bioresorbable sensor (via data acquisition (DAQ) system USB-4065, National Instruments, USA) with pressures from the commercial sensor yielded calibration curves. Additional data appear in Supplementary Information.

**Connections to wireless data-transmission systems.** Laser cutting of foils of molybdenum ( $\sim 10$   $\mu$ m thick) or magnesium ( $\sim 50$   $\mu$ m thick) yielded dissolvable narrow metal strips (that is, interconnection wires,  $80$   $\mu$ m  $\times$   $30$  mm). Pressing these wires against PLGA substrates using a PDMS stamp at 65 °C embedded them into the surface of the PLGA. Sputter deposition of molybdenum ( $\sim 2$   $\mu$ m) through high-resolution stencil masks (12.5  $\mu$ m, Kapton; Dupont, USA) yielded electrical connections between the wires and contact pads on the PLGA (Supplementary Fig. 20). The opposite ends of the wires connected to externally mounted wireless communication systems (Pinnacle Technology, USA) (Supplementary Fig. 21).

**Evaluation of the kinetics of device dissolution.** Measurements of time-dependent changes in the thicknesses of square ( $100$   $\mu$ m  $\times$   $100$   $\mu$ m) Si-NMs ( $\sim 200$  nm thick), electron-beam evaporated layers of SiO<sub>2</sub> ( $\sim 100$  nm), free-standing nanoporous silicon substrates (np-Si,  $\sim 80$   $\mu$ m) and magnesium foils ( $\sim 80$   $\mu$ m) due to immersion in ACSF at body temperature (37 °C) established the dissolution kinetics of the key materials. Removing samples from the ACSF every other day, rinsing them with deionized water, and measuring the thicknesses by profilometry (Dektak, USA) yielded the dissolution rate, as in Supplementary Fig. 16. Sealed reservoirs of PDMS with viewing windows allowed for observation of dissolution behaviour at the level of the completed devices. These engineered structures included access channels around the periphery to allow passive fluid exchange and diffusion with a surrounding bath (Supplementary Fig. 17).

**Evaluation in animal models.** Studies were performed in strict accordance with the recommendations in the Guide for the Care and Use of Laboratory Animals of the National Institutes of Health. The protocol was approved by the Institutional Animal Care and Use Committee (IACUC) of Washington University in St Louis (protocol number 20140207). Male Lewis rats weighing 250–350 g (Charles River, Wilmington, MA) received subcutaneous injections of buprenorphine hydrochloride ( $0.05$  mg kg<sup>-1</sup>; Reckitt Benckiser Healthcare Ltd, USA) for pain management, and of ampicillin ( $50$  mg kg<sup>-1</sup>; Sage Pharmaceuticals, USA) to prevent infection at the implantation site before the surgical process. Animals were anaesthetized with isoflurane gas and held in a stereotaxic frame for the duration of the surgical procedure and measurements. Opening a craniectomy and dural, implanting bioresorbable sensors on the cortical surface, sealing the craniectomy with a PLGA sheet ( $\sim 80$   $\mu$ m thick) and/or biodegradable surgical glue, and suturing the skin implanted the fully resorbable biosensing system in intracranial space. Comparison testing with a clinical intracranial pressure sensor (Integra LifeSciences, USA) and commercial thermistor (DigiKey Electronics, USA) implanted in parallel to bioresorbable sensors demonstrated the functionality of the bioresorbable sensors. To implant the injectable device, the same procedure of opening a craniectomy and dural was performed. Injecting needle-shaped biosensors into the brain parenchyma ( $\sim 5$  mm deep) with a stereotaxic frame and arm enabled monitoring of

pressure and temperature in the deep-brain parenchyma. Additional details on the manual operation of pressure/temperature changes, the immunohistochemistry tests, and the surgical process and measurement at the intra-abdominal cavity and lower extremities appear in Supplementary Information. The immunohistochemistry tests used five individual rats per stage (2, 4 and 8 weeks) and device type (np-Si and magnesium-foil substrates). *In vivo* functionality tests of pressure and temperature sensors involved three trials using different batches of devices and animals, to establish reproducibility.

**Implantable near-field-communication wireless system.** The sensor introduced in Fig. 2a can be integrated with sub-dermal wireless data-transmission systems, constructed largely of bioresorbable materials, via thin, bioresorbable wires that pass through the skull. Extended Data Fig. 1a and b show an illustration of a chip-scale, near-field-communication (NFC) technology that includes bioresorbable coils, polymer substrates, encapsulation layers and resistors, a partially bioresorbable NFC chip, and non-resorbable capacitors, and a picture of this system integrated with a bioresorbable pressure sensor via biodegradable wiring. Here, micro-patterned magnesium coils ( $50$   $\mu$ m thick, outer diameter  $15$  mm) allow inductive coupling to an external data reader for power transfer and data transmission. A silicon-based logic chip (RF430FRL152H, Texas Instruments, USA;  $4$  mm  $\times$   $4$  mm  $\times$   $\sim 300$   $\mu$ m) captures the measured data at a high acquisition rate, then digitizes and processes the information for transmission to the external reader. Passive components include Si-NM resistors and capacitors. PLGA serves as the substrate and electrical passivation layer. Extended Data Fig. 1c summarizes the operating principles. The external reader wirelessly delivers power for operating the logic chip and provides the small currents needed to assess the response of the piezoresistive and thermoresistive sensors. In particular, changes in resistance associated with changes in pressure and temperature register as voltages that can be recorded and transmitted to the external reader by the NFC chip through the associated coil antenna. This NFC system is far more sophisticated than a conventional radio-frequency-identification (RFID) tag. Here, a single chip platform provides all of the computing functionality needed for high-speed data recording, real-time software filtering, and wireless transmission of sensor outputs as captured with an on-board 14-bit analogue-to-digital converter.

This system communicates through biofluids and tissue with little loss, owing to the use of magnetic coupling in a relatively low-frequency band (13.56 MHz; Supplementary Fig. 32), consistent with negligible heating associated with system operation (Supplementary Fig. 33). These characteristics enable communication distance of up to 25 mm through biological tissue. The high-speed, programmable operation of the NFC chip is critical to overall operation. Supplementary Fig. 34a presents examples of data-acquisition rates of up to 250 Hz, via recordings of oscillating voltages (sine wave) with frequencies from 1 Hz to 50 Hz. Spectrograms and other related data appear in Supplementary Fig. 34b–d. These high sampling rates allow efficient operation of digital filtering algorithms, and they also foreshadow the ability to measure biosignals such as EEG, ECoG and ECG. Supplementary Fig. 35 demonstrates the response of real-time high/low-pass filter function achieved by software programming for on-board computation with the NFC chip. Supplementary Fig. 36 shows two-channel operation of the system with/without this type of filtering during sensing. This integrated system provides wireless operation that compares quantitatively with that of a commercial wired sensor (Supplementary Fig. 37).

The wireless module is largely bioresorbable, as illustrated in Extended Data Fig. 1d through images at various stages of dissolution in ACSF at 60 °C. The magnesium coils, electrodes, interconnects and silicon resistors (240 mg;  $\sim 85\%$  of the total mass of the NFC system) dissolve fully after 14 days. Here, the NFC chip is not bioresorbable; but fully bioresorbable complementary metal-oxide semiconductor (CMOS) circuit technologies offer the potential for constructing bioresorbable chips. In particular, recently reported schemes demonstrate that modest modifications to otherwise conventional semiconductor-manufacturing techniques allow the use of foundry fabrication facilities for construction of bioresorbable CMOS<sup>34</sup>. Even with the examples presented here, where the NFC chip is not fully bioresorbable, the associated implantation strategy minimizes risk by locating the hardware subdermally on the skull, outside the intracranial space, thereby allowing rapid, facile extraction.

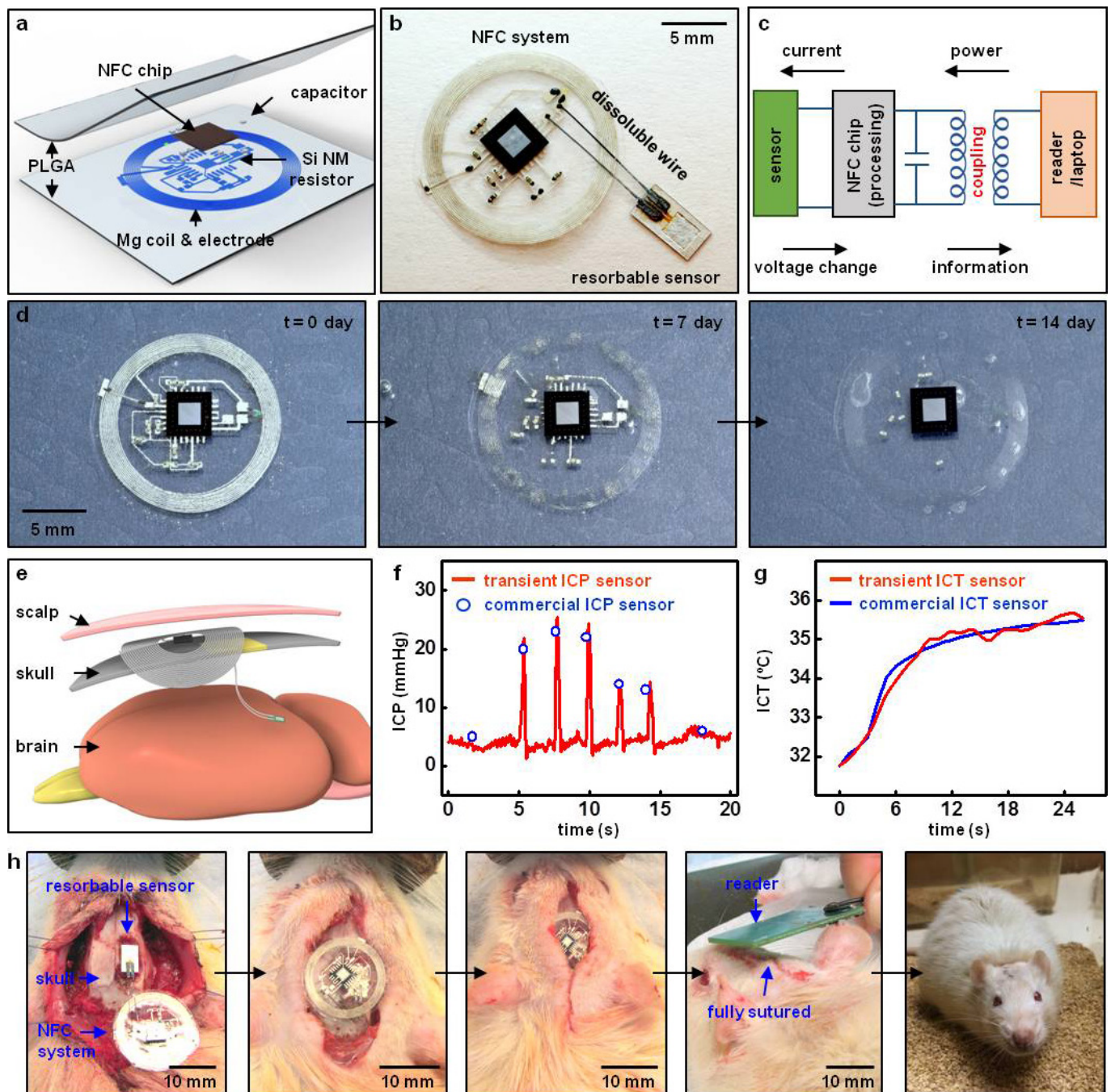
In this overall architecture, the fully bioresorbable sensors reside in the intracranial space, while the NFC system resides extracranially within the subgaleal layer of the scalp. Fine, dissolvable wiring provides electrical interconnections through a burr hole in the skull, sealed with a bioresorbable surgical glue. After completing the subgaleal closure, the wireless system and sensor are fully implanted. Extended Data Fig. 1e–h show a diagram of the implantation strategy, surgical process, and wireless *in vivo* intracranial pressure and temperature results measured in a rat model. Here, all of the components in the intracranial region are fully bioresorbable. The non-bioresorbable components of the system remain extra-axial within the

scalp, thereby minimizing the risk of provoking pathological neuroinflammation in the intracranial space. In addition, the relative material safety (as judged by the US Food and Drug Administration (FDA) class) of, for example, a subdermally implanted encapsulated non-resorbable device (such as an RFID chip) is similar to that of a titanium fixation screw. Removal of an extra-axial component involves a much lower risk than intracranial surgery. Intracranial pressure and temperature values measured in the rat model using the NFC system are comparable to those captured using commercial wired sensors.

**Fabrication of a fully implantable NFC wireless system.** The magnesium foil was patterned on the PDMS by using photolithography and etching with dilute hydrochloric acid (deionized water:HCl = 15:1). Transfer printing of the patterned magnesium foil onto a film of PLGA (~150 μm) formed the inductive coil and

electrode. The Si-NM resistor was formed on the SOI wafer by doping with phosphorus at 950 °C and patterning the top silicon (~300 nm thick) into the trace. Undercutting the buried oxide with hydrofluoric acid and transfer printing Si-NM on PLGA formed the resistor of NFC system. Laminating the top PLGA (~150 μm) and heating it at 65 °C yielded the passivation layer. Biodegradable conductive W paste served to interconnect the NFC wireless system to the metal wire (molybdenum or magnesium)<sup>35</sup>.

34. Yin, L., Bozler, C., Harburg, D. V., Omenetto, F. & Rogers, J. A. Materials and fabrication sequences for water soluble silicon integrated circuits at the 90 nm node. *Appl. Phys. Lett.* **106**, 014105 (2015).
35. Huang, X. *et al.* Biodegradable materials for multilayer transient printed circuit boards. *Adv. Mater.* **26**, 7371–7377 (2014).



**Extended Data Figure 1 | Fully implantable near-field communication (NFC) system with bioresorbable interface and intracranial sensors.**

**a**, Diagram of a fully implantable NFC system. This device uses a magnesium foil ( $\sim 50\ \mu\text{m}$ ) for the inductive coil, interconnects and electrodes; patterned silicon nanomembranes (Si-NMs,  $\sim 300\ \text{nm}$ ) for resistors; conventional capacitors; and an advanced NFC microchip for data acquisition, processing and transmission. PLGA serves as the substrate and for encapsulation. The diameter of the entire device is about 15 mm. **b**, Image of this type of NFC system integrated with a bioresorbable pressure sensor. **c**, Diagram of the operational principles. **d**, Series of images showing accelerated dissolution of the NFC system

inserted into an ACSF at  $60^\circ\text{C}$ . **e**, Diagram of the implantation process. The bioresorbable sensors reside in the intracranial space, while the NFC system is located extracranially, on the outside surface of the skull, beneath the skin. Bioresorbable, thin metal wires interconnect the NFC system and the sensors. **f**, Real-time wireless measurements of ICP, showing transient increases induced by the Valsalva manoeuvre (red, data obtained from a transient ICP sensor; blue, data obtained from a commercial ICP sensor). **g**, Increase in ICT owing to application of a heating blanket around the head, as determined by bioresorbable (red) and commercial (blue) sensors. **h**, Demonstrations of implantation and suturing in a rat model. A biodegradable surgical glue (TISSEAL) seals the intracranial space.

## Table of Contents

<b>Supplementary Methods and Discussion</b>	page
1. Fabrication of nanoporous Si (or Mg foil) trench	2
2. Calibration of biodegradable biosensors	2
3. Operating principles of mechanical/physical/chemical sensors	4
4. Temperature effects on piezoresistivity of pressure sensors	6
5. Animal behavior test with percutaneous wires	8
6. <i>In vivo</i> implantation of bioresorbable wireless monitors for intracranial pressure and temperature	8
7. Characterization of near-field communication (NFC) system	10
8. Synthesis/hydrolysis chemistry, dissolution kinetics, water permeability, biocompatibility of polyanhydride encapsulation	10
9. Immunohistochemistry	13
10. Other applications of bioresorbable pressure sensors	14
11. Injectable biodegradable sensors	15
12. Characterizations of porosity and average pore size of nanoporous silicon (np-Si)	15
Reference	17
Supplementary Figures and Legends S1 – S27	19

## **1. Fabrication of nanoporous Si (or Mg foil) trench**

Nanoporous Si (np-Si) and Mg foil served as mechanical supports for microelectromechanical systems (MEMS). Free-standing np-Si (~80  $\mu\text{m}$  thick) was prepared from double-side polished, highly doped p-type Si wafers (0.001-0.005  $\Omega\cdot\text{cm}$ , University Wafers, USA) at a current density 160  $\text{mA}\cdot\text{cm}^{-2}$ , as previously reported.<sup>1</sup> Lamination delivers the np-Si onto a layer of PDMS spin cast on a glass slide, for deposition of  $\text{SiO}_2$  (~300 nm) by PECVD. Patterning and etching of the  $\text{SiO}_2$  and np-Si yielded a trench in the np-Si. As an alternative to np-Si, a commercial Mg foil (~100  $\mu\text{m}$  thick, Goodfellow, USA) can be thinned, patterned, and wet etched by a mixture of acetic acid ( $\text{CH}_3\text{COOH}$ , Transene Company Inc., USA) and deionized (DI) water (20 ml: 250 ml), to create a trench (~40  $\mu\text{m}$  depth) in the processed Mg foil (~80  $\mu\text{m}$  thick). The PLGA is transfer printed on the np-Si (or Mg foil) with a micro-tip patterned PDMS stamp.<sup>2</sup> The manufactured devices on PLGA substrates were then integrated with np-Si (or Mg foil) near the glass transition temperature ( $T_g$ , ~65 °C) for 5 min on a hot plate.

## **2. Calibration of biodegradable biosensors**

***Accelerometer*** — Calibration involved measurements of a biodegradable accelerometer and a commercial device (NeuLog, USA) moved rapidly up and down in the vertical direction. The calibration approach to connect measured changes in resistance to acceleration was similar to that used for the pressure sensor. ***Temperature sensor*** — Real-time measurements of the change in resistance of a biodegradable sensor and of temperature using a commercial sensor (NeuLog, USA) submerged in ACSF yielded the

calibration curves (Fig. S10). **Flow meter** — The device was placed in a water bath with constant flow rate. While 1 mA (DC current source; Model 6220, Keithley, USA) was applied to the thermal actuator, the resistances of the two temperature sensors were measured using a data acquisition (DAQ) system (USB-4065, National Instruments, USA). **Thermal conductivity/diffusivity sensor** — The thermal conductivity of an aqueous solution was measured as follows. A current (500  $\mu$ A) was supplied to the resistive element by a programmable DC current source (Model 6220, Keithley, USA) for 1 s. The time-dependent voltage across the element was then sampled at 100 V/s using a 22-bit programmable digital multimeter (USB-4065, National Instruments, USA). The voltage and current values allowed calculation of the time-dependent resistance of the device, which, in turn, is proportional to temperature. **pH sensor** — Si nanoribbons (Si NRs) were exposed by ultraviolet induced ozone for 3 min and immersed in a 1% ethanol solution of 3-aminopropyltriethoxysilane (APTES, Sigma-Aldrich, USA) for 20 min. After thorough rinsing with ethanol three times, Si NRs were annealed at 60°C for 10 min to functionalize their surfaces. An Ag/AgCl reference electrode was placed in the center of the solutions, and a floating gate voltage defined the quiescent conductance of the Si NRs. Changes in conductance were measured during partial immersion of the device in phosphate buffer solution (Sigma Aldrich, USA) with various pH between 2 and 10. After a short period of stabilization, a semiconductor analyzer (4155C, Agilent, USA) recorded the conductance of the Si NRs for ~50 s in the solutions.

### **3. Operating principles of mechanical/physical/chemical sensors**

**Pressure sensor** — The deformable diaphragm structure in Figure 1a provides a highly sensitive pressure response.<sup>3,4</sup> The average strain in the Si-NM serpentine structure on PLGA induced by applied pressure causes a piezoresistive electrical response. Under intracranial pressure, both the np-Si mechanical support and PLGA diaphragm would deform. Three-dimensional finite element analysis (3D-FEA), however, suggests that the deformation of the np-Si mechanical support is negligible in comparison to that of PLGA diaphragm, indicating a reasonable simplification to clamp all four edges of PLGA diaphragm in the current study.<sup>5</sup> In the numerical analysis, an 8-node hexahedral solid element C3D8R and a quadrilateral shell element S4R were used for the diaphragm and Si-NM piezoresistive sensor, respectively. The ideal elastic constitutive relation describes the mechanical behavior of the Si and PLGA. To maximize the sensor sensitivity (i.e., average strain in the Si-NM piezoresistive sensor) to applied pressure, the center of the edge of the diaphragm was chosen as the location for the sensor. The average strain at different positions of diaphragm shown in Fig. S5 rationalizes this choice. The sensitivity also depends on the size of PLGA diaphragm. For a given area, 3D-FEA results indicate that the optimum is achieved when the PLGA diaphragm is close to a square in shape (see Fig. S6). Fig. S7 provides a comparison of experimental and FEA results for change in resistance with pressure. The following equation provides the relationship between the change in resistance due to piezoresistivity through a gauge factor ( $G$ ):

$$R = R_0(1 + G\varepsilon), \quad (1)$$

where  $\varepsilon$  is the average strain on the piezoresistive sensor, and  $R$  and  $R_0$  are the change in resistance and resistance at zero pressure, respectively. Here, the average strain was calculated from 3D-FEA for pressure ranging from 0 to 70 mmHg. With  $R_0$  as 249

$k\Omega$ , the gauge factor was estimated to be  $\sim 30$ . **Accelerometer** — The pressure sensor platform can serve as an accelerometer where the sensor consists of a cantilever with a rigid proof mass  $m$  attached at its distal end (Fig. S11). Under a given acceleration  $a$ , the force experienced by the proof mass generates a bending moment at the fixed end of the beam,  $M = mad$ , where  $d$  is the distance from the center of the proof mass to the fixed end. This results in a strain at the location where Si-NM piezoresistive coil resides  $\varepsilon = Mt/(2EI)$ , where  $EI = Ewt^3/12$  is the bending stiffness of the cantilever, and  $w$  and  $t$  are the width and thickness of the cantilever, respectively. Taken together with Equation (1), the acceleration sensitivity is tunable by changes of the elastic properties and the geometry via the following relationship  $a = \Delta R/R(Ewt^2)/(6Gmd)$ .<sup>3,6</sup> **Temperature sensor** — The resistance (or conductance) changes by an amount linearly proportional to temperature, according to:

$$R = R_0(1 + \alpha(T - T_0)) \quad (2)$$

where  $R$  and  $R_0$  are the changed resistance and initial resistance,  $T$  and  $T_0$  are the measured and initial temperatures, and  $\alpha$  is the temperature coefficient of resistance (TCR). The TCR in Figure 1h is  $1 \times 10^{-4}$ , where doped Si has various TCR ranges depending on the type of dopants and doping concentration.<sup>7</sup> A larger initial resistance increases the absolute change in resistance. As a result, highly dense serpentines, which dominate the total resistance, were adopted for the temperature sensors (see Fig. S12). **Flow rate monitor** — The flow rate monitor consists of one thermal actuator and two temperature sensors (see Fig. S14). The thermal actuator is placed in the middle of two temperature sensors, along the flow direction. When the actuator generates heat, a temperature difference appears between two temperature sensors, due

to heat transfer mediated by the flow.<sup>8</sup> The difference in temperature can be quantitatively correlated to flow rate. **Thermal conductivity/diffusivity sensor** — A sudden increase of the power applied to the resistive element induces a temperature increase in the resistor due to Joule heating. The time dynamics of the temperature increase is, in part, a function of the thermal transport properties of the surrounding fluid. As a result, analysis of the temperature transients immediately following the power increase allows determination of the thermal transport properties of the surrounding fluid or tissue.<sup>9</sup> **pH sensor** — The functionalized surfaces of Si-NRs with both  $-\text{NH}_2$  and  $-\text{SiOH}$  groups undergo protonation to  $-\text{NH}_3^+$  at low pH and deprotonation to  $-\text{SiO}^-$  at high pH.<sup>10-12</sup> The resulting changes in the surface charge electrostatically gate the transport in the Si-NRs by depleting or accumulating charge carriers, resulting in a stepwise decrease in the conductance of the phosphorous-doped Si-NRs as the pH in aqueous solutions increases from 2 to 10 in distinct steps (see Fig. S15 for Si pH sensor).

#### **4. Temperature effects on piezoresistivity of pressure sensors**

Temperature affects the resistance and the coefficient of piezoresistivity.<sup>7</sup> Therefore, calibration of these effects in piezoresistive-type pressure sensors enhances the accuracy of the pressure measurements. The temperature effect on resistance is described by Equation (2) in the previous section through the temperature coefficient of resistance (TCR,  $\alpha$ ). The temperature effect on piezoresistivity is described by the temperature coefficient of piezoresistivity (TCP,  $\beta$ )

$$\pi = \pi_0(1 + \beta(T - T_0)), \quad (3)$$

where  $\pi$  and  $\pi_0$  are the final and initial piezoresistivity coefficients, and  $T$  and  $T_0$  are the measured and initial temperatures, respectively. The temperature coefficient of piezoresistivity  $\beta$  of Si varies, depending on the dopants and doping concentration.<sup>7</sup> Assuming the piezoresistivity is directly proportional to the gauge factor ( $G$ ), the strain ( $\varepsilon$ ) can be correlated with resistance (TCP) as

$$R_{(T,P)} = R_{(T,P=0)} (1 + G\varepsilon) = R_{(T=0,P=0)} [1 + \alpha(T - T_0)] \{1 + G_0 [1 + \beta(T - T_0)] \varepsilon\} \quad (4)$$

where  $R_{(T,P)}$  is the final resistance affected by temperature and pressure,  $R_{(T,P=0)}$  is the resistance when only temperature is applied,  $R_{(T=0,P=0)}$  is the initial resistance without changes in pressure nor temperature (usually 20 or 25 °C),  $G$  and  $G_0$  are the final and initial gauge factors. With predetermined  $\alpha$ ,  $\beta$ ,  $G_0$  and  $R_{(T=0,P=0)}$ , the temperature effects on the resistance and piezoresistivity can be calibrated. Fig. S19 shows the resistance vs. pressure curve at the different temperatures measured by transient pressure sensors, giving  $\alpha=0.5 \times 10^{-3}$  and  $\beta=-2.2 \times 10^{-3}$ . It should be noted that a typical range of  $\beta$  of p-type Si is  $-2.7 \times 10^{-3}$  to  $-1.6 \times 10^{-3}$ , for doping concentration between  $5 \times 10^{18}$  and  $1 \times 10^{20}/\text{cm}^3$ .<sup>7</sup> Here the change in pressure sensitivity due to temperature change in this intracranial study ( $\pm 5$  °C) is about 1%, and hence negligible. The following simplified equation can then be used to calibrate the temperature effect on the base resistance:

$$R_{(T,P)} = R_{(T=0,P=0)} [1 + \alpha(T - T_0)] (1 + G_0 \varepsilon). \quad (5)$$

Optimizing the doping concentration to increase the sensitivity to pressure and minimize sensitivity to temperature, and/or using a Wheatstone-bridge type of design with four piezoresistive elements, are alternative routes to minimize the temperature effect.<sup>3,4</sup>

### **5. Animal behavior test with percutaneous wires**

The novel object recognition (NOR) task is used to evaluate cognition, particularly recognition memory, in rodent models of CNS disorders. We tested 6 controls and 6 rats with implanted percutaneous wires and their spontaneous tendency to spend more time exploring a novel object than a familiar one. The choice to explore the novel object reflects the use of learning and recognition memory. We observed no significant change in those with precautions implants as opposed to controls as shown in Figure S31.

### **6. *In vivo* implantation of bioresorbable wireless monitors for intracranial pressure and temperature**

Animals were anesthetized and held in a stereotaxic frame after analgesia and antibiotic prophylaxis. Incising along the dorsal midline of the head longitudinally and retracting the scalp allowed the visualization of bregma and lambda. The craniectomy was fashioned utilizing a high speed drill on the right side of the rat's skull over somatosensory cortex. After placing the transient biosensors on the cortical surface, small pieces of saline soaked absorbable gelatin compressed sponge (Gelfoam®, Pfizer, USA) were applied. For the fully implantable NFC system, the craniectomy defect was sealed by degradable surgical glue (TISSEEL, Baxter Healthcare Co., USA), and the NFC system was placed on the outside surface of the skull. A subgaleal closure utilizing interrupted resorbable sutures sealed the surgical site with all device components fully implanted. For the transcutaneous bioresorbable wiring method,

placing a PLGA sheet on the skull by covering the craniectomy defect and bonding the sides by degradable surgical glue formed the closed intracranial cavity while the wires were withdrawn outside. Finally, a subgaleal closure utilizing interrupted resorbable sutures while laying degradable wires out provides the fully resorbable interfaces with dissolvable metal wires. The plastic hat, which provides the protection from rat's movement and handling, was bonded on the sutured region with an epoxy. Placing a wireless transmitter (Pinnacle 8151 fixed-frequency 2-channel wireless potentiostat, Pinnacle Technology, USA) with connection of the degradable wires in the plastic hat allows the long range (>10 m) wireless monitoring of pressure and/or temperature. The battery-powered potentiostat delivered a 0.6 V potential to each channel at a 1 Hz sampling frequency, measured and amplified the delivered current with a gain of 100,000 digitized the reading, and transmitted the value over a 900 MHz wireless protocol to a computer-connected base station. Implanting a standard clinical ICP monitor, (Integra LifeSciences Co., USA) near the dissolvable sensor and sealing with a silicone polymer enabled the comparison of resorbable pressure sensor with a clinical ICP monitor. The commercial thermistor (DigiKey Electronics, USA) implanted at the site near the resorbable temperature sensor and plugged to a wireless transmitter provided the parallel monitoring of brain temperature with resorbable sensor. Post-operative care procedure based on the local protocol of the animal welfare regulations providing the rat's reasonable recovery and health movement in single-housed cage.

## **7. Characterization of the near-field communication (NFC) system**

The NFC chip operates using power delivered wirelessly by inductive coupling. The regulated working voltage ranges from 1.45 to 1.65 V. The chip includes a microcontroller (MSP430), with 2kB, 4kB and 8kB of FRAM, SRAM and ROM, respectively. The system supports four channels of Sigma-Delta analog to digital converters, each with 14 bit resolution. The phase, impedance, and resonance frequency of the fully implantable NFC system was evaluated by near field coupling to a coil connected to an impedance analyzer (Agilent 4191A RF Impedance Analyzer, Agilent, USA). A signal generator (Keithley 3390, Keithley, USA) provides 10 Hz sine, square, ramp wave inputs to the NFC system, The input of the signal generator and the wireless measured signals from the NFC system were compared to assess the high speed acquisition capabilities. Finite impulse response filters were loaded into the chip and frequency responses were acquired by using the signal generator to produce sine wave inputs with frequencies between 0.1 to 20Hz.

## **8. Synthesis/hydrolysis chemistry, dissolution kinetics, water permeability, biocompatibility of polyanhydride encapsulation**

A biodegradable polyanhydride, PBTPA (poly buthanedithiol 1,3,5-triallyl-1,3,5-triazine-2,4,6(1H,3H,5H)-trione pentenoic anhydride), was synthesized and used as an organic encapsulant, capable of defining the lifecycle of device operation by controlling the water diffusion. Thiol-ene click-chemistry was used for the construction of degradable polyanhydride. Mixture of 1 mole of 4-pentenoic anhydride (4PA), 4 mole of 1,3,5-triallyl-1,3,5-triazine-2,4,6(1H,3H,5H)-trione (TTT)

and 7 mole of 1,4-butanedithiol was polymerized by UV light for an hour with the addition of 2-hydroxy-4'-(2-hydroxyethoxy)-2-methylpropiophenone as the photoinitiator (total mass of 0.1%), yielding biodegradable PBTPA with hydrophobic chains (see Fig. S23). Here, 4PA and TTT act as a degradable linker and hydrophobic component, respectively, and butanedithiol crosslinks both 4PA and TTT through UV induced thiol-ene reaction.

Fig. S24a shows the hydrolysis kinetics of polyanhydride at the different solution pH at room temperature, 0.5, 1.2, 2.8 mg/day for pH 6.7, 7.4, and 8 solutions. Since anhydride bonds can be hydrolyzed giving two hydrophilic carboxylic acid bonds, PBTPA tends to gradually collapse and dissolve into water (see Fig. S23). The water permeability can be tracked by a simple water-sensitive electrical element, i.e. an Mg resistor in this study. The resistance of the Mg resistor increases if the water diffuses to the Mg and begins to dissolve it. Details of this type of test method appear elsewhere.<sup>13,14</sup> Fig. S24b shows the resistance at various times for a Mg resistor (~300 nm thick) encapsulated with polyanhydride (~120  $\mu\text{m}$ ). The Resistance is stable until 4 days and then starts to increase significantly, implying the Mg resistor has dissolved. Polyanhydride provides a barrier to water diffusion to control the operating lifetime of the pressure sensor. This type of electrical degradation is observed in the encapsulation of the interconnecting electrodes (Mo). Fig. S27 shows the degradation of electrical function of biodegradable wires (Mo, Mg) and interconnecting electrode (Mo) measured without encapsulation. The Mg wires are stable for about 5 days (change of less than 3  $\Omega$ ) but then shows large changes in resistance, due to their increased rate of dissolution compared to Mo (which shows a much smaller resistance change, ~3  $\Omega$ ). The Mo electrode parts dissolve within a few hours without encapsulation.

Polyanhydride encapsulation enhances the stable operation time of Mo to six days with less than 10  $\Omega$  change. At 7 days the water begins to dissolve the Mo interconnection significantly and the resistance increases to  $\sim 50 \Omega$ .

An additional layer of encapsulation on the PLGA membrane affects the mechanics of deformation, thereby changing the calibration. Fig. S22a indicates a change from 82 to 50  $\Omega/\text{mmHg}$  via the addition of a 120  $\mu\text{m}$  thick coating of polyanhydride. Fig. S22b summarizes results of FEA simulation, consistent with this observation. The average strain in the Si-NM sensor reduces with the addition of the encapsulation. The balance between sensitivity and operational lifecycle can be managed through appropriate selection of trench geometry, Si-NM width, modulus and thickness of the membrane and the encapsulation layer, and the water permeation (chemistry and thickness of encapsulation).

Pieces of polyanhydride (10 mm  $\times$  3 mm) and HDPE (High-density polyethylene, negative control sample) were implanted subcutaneously in Balb/c mice to assess the toxicity. Fig. S25 provides hematoxylin and eosin (H&E) images of tissue around the implant sites for polyanhydride and HDPE after 14 days. Histologic examination showed that inflammatory cell infiltration and fibrosis in surrounding tissues were no different with negative control groups. There were no obvious signs of local toxicity caused by polyanhydride or its by-products as results were comparable to the HDPE group.

## **9. Immunohistochemistry**

Immunohistochemistry was performed as described previously, with minor modifications.<sup>15,16</sup> The two types of bioresorbable pressure sensors (np-Si and Mg foil structure) were placed on the cortex in the craniectomy site on the right hemisphere above the sensory motor cortex for 2 weeks, 4 weeks, and 8 weeks. A craniectomy is performed on the left side again above the sensorimotor cortex and the dura is opened above the sensorimotor cortex but no implant is placed. This acts as a histological control to the right side with the implant placed. Brain slices are double-immunostained for GFAP (glial fibrillary acidic protein) to detect astrocytes and Iba1 (ionized calcium-binding adapter molecule 1) to identify microglia/macrophages. Briefly, rats are anesthetized and intracardially perfused with ice-cold 4% paraformaldehyde in phosphate buffer (PB). Brains are carefully dissected with particular attention to preserve the right cortical surface beneath the now fully resorbed device and the left cortical surface acting as a control. Brains are post-fixed 2 hr at 4 °C and cryoprotected with solution of 30% sucrose in 0.1M PB at 4°C for at least 4 d, cut into 30 µm sections and processed for immunostaining. 30 µm brain sections are washed three times in PBS and blocked for one hour in PBS containing 0.5% Triton X-100 and 5 % normal goat serum. Sections are then incubated for 16 hr at 4°C in guinea pig anti-GFAP (1:500, Synaptic Systems 173 004) and rabbit anti-Iba1 (1:300, Wako Chemicals 019-19741). Following incubation, sections are washed three times in PBS and then incubated for 2 hr at room temperature in Alexa fluor 488 goat anti-rabbit IgG (1:1000, Life Technologies A11008) and Alexa fluor 546 goat anti-guinea pig IgG (1:1000, Life Technologies A11074). Sections are then washed three times in PBS and then incubated for 1 hr at room temperature in NeuroTrace® 435/455 Blue Fluorescent Nissl Stain (Life Technologies N21479) in PB (1:400). Sections are then washed three times in

PBS followed by three washes in PB and mounted on glass slides with HardSet Vectashield (Vector Labs) for microscopy. All sections imaged on a digital slide scanner (Olympus NanoZoomer HT model). Gain and exposure time are digitally set and constant throughout. Images corresponding with the right cortical surface interfacing with the device are compared with the left control cortical surface which did not have a device implanted. Gliosis is compared between cortex underlying the now resorbed implant and the control.

### **10. Other applications of bioresorbable pressure sensors**

Sensors implanted at the intra-abdominal cavity and lower extremities demonstrated the versatility usages in implantable biomedical applications. The abdominal wall was shaved and prepped at the incision site with 70% ethanol. Animals were subjected to a 4 cm full-thickness median incision along the linea alba, using the xiphoid process as the reference point by a sterile technique. After abdominal incision, the transient pressure sensor and clinical pressure sensor were placed in the abdominal cavity amongst the abdominal viscera. A modified roman sandal technique using a 3/0 VICRYL RAPIDE (polyglactin 910) suture secured the sensor and the abdomen was closed with simple interrupted 3/0 VICRYL RAPIDE (polyglactin 910) sutures. Manual abdominal compression yielded the increase of intra-abdominal pressure. A small (~5 mm) vertical incision was made along the thigh using scissors, and the skin was retracted laterally to implant the pressure sensor into extremities cavity. The muscles of the posterior thigh (including the hamstring

muscles) were split, and the biodegradable pressure sensor and commercial sensor were placed in the musculofascial compartment. The implants were secured utilizing the same method as the abdominal surgery.

### **11. Injectable biodegradable sensors**

A three-axis vertical stereotactic frame and arm temporary tied with an injectable device allowed accurate positioning and stable injection into the deep brain site. Adjustments of the jig enabled the needle system to penetrate into brain tissue via a square hole in the skull of a rat. Release of the needle device completed implantation, followed by sealing the skull with a silicone polymer (Kwik-Sil, World Precision Instruments Inc., USA) and dental acrylic. A manual increase in pressure induced by compressing the abdomen provided a means to compare the bioresorbable needle pressure sensor to a commercial device injected at an adjacent location. Monitoring the temperature during the anesthetization and recovery yielded data to compare the bioresorbable temperature sensor to temperatures measured by infrared imaging on the surface of brain.

### **12. Characterizations of porosity and average pore size of nanoporous silicon (np-Si)**

The porosity of the np-Si was characterized by optical reflectance spectroscopy. The refractive index of np-Si ( $n$ ) was determined as  $\sim 1.55$  from the spacing of adjacent maxima in the Fabry-Perot oscillations in the reflectance spectrum ( $\sim 1.3$  to  $1.6 \mu\text{m}$ )

using<sup>17</sup>

$$n = \frac{1}{2d} \cdot \frac{1}{\left( \frac{1}{\lambda_1} - \frac{1}{\lambda_2} \right)}, \quad (6)$$

where  $\lambda_1$  and  $\lambda_2$  are the local maximum and the adjacent, longer-wavelength local maximum in the reflectance spectrum, and  $d$  is the thickness of np-Si determined by scanning electron microscope (SEM). The porosity was determined by using the calculated  $n$  and the two-component Bruggeman effective medium approximation:<sup>18</sup>

$$\phi \left( \frac{1-n^2}{1+2n^2} \right) + (1-\phi) \left( \frac{n_{Si}^2 - n^2}{n_{Si}^2 + 2n^2} \right) = 0, \quad (7)$$

where  $\phi$  and  $n_{Si}$  are the porosity of np-Si and the real part of the refractive index of bulk Si, respectively.<sup>19</sup> Assuming a Si bulk refractive index of 3.5, the porosity of np-Si is  $\sim 70.5\%$ . This agrees well with gravimetric porosity measurements (i.e. relative mass of np-Si film to mass of bulk Si that would occupy the same geometric volume), which suggest an average porosity of  $69 \pm 3\%$ .

The average pore size was determined using a gas sorption system (NOVA *-e* Series, Quantachrome Instruments). np-Si membranes were subjected to both nitrogen adsorption and desorption measurements. The sorption system's NovaWin software applied the Barrett, Joyner, and Halenda (BJH) Method<sup>20</sup> to the experimental isotherms, resulting in an average pore size of  $12 \pm 3$  nm, which is in agreement with what is observed in the top view image from the scanning electron microscope.

## References

1. Ning, H. *et al.* Transfer-Printing of Tunable Porous Silicon Microcavities with Embedded Emitters. *ACS Photonics* **1**, 1144–1150 (2014).
2. Wu, J. *et al.* Mechanics of reversible adhesion. *Soft Matter* **7**, 8657–8662 (2011).
3. Liu, C. *Foundations of MEMS* Ch. 6 (Prentice Hall, London, 2011).
4. Sugiyama, S., Takigawa, M., Igarashi, I. Integrated Piezoresistive Pressure Sensor with Both Voltage and Frequency Output. *Sens. and Actuators A* **4**, 113–120 (1984).
5. Wang, C.-T., *Nonlinear large-deflection boundary-value problems of rectangular plates*. (DTIC Document, 1984).
6. Angell, J.B., Terry, S. C., Barth, P.W. Silicon Micromechanical Devices. *Sci. Am. J.* **248**, 44–55 (1983).
7. Hsu, T. R. *MEMS & Microsystems: Design, Manufacture, and Nanoscale Engineering* Ch. 7 (John Wiley & Sons, Inc., Hoboken, New Jersey, USA, 2008).
8. Van der Horst, A. *et al.* A Novel Flexible Thermoelectric Sensor for Intravascular Flow Assessment. *IEEE Sens. J.* **13**, 3883–3891 (2013).
9. Webb, R. C. *et al.* Ultrathin Conformal Devices for Precise and Continuous Thermal Characterization of Human Skin. *Nature Mater.* **12**, 938–944 (2013).
10. Vezenov, D. V., Noy, A., Rozsnyai, L. F., Lieber, C. M. Force titrations and ionization state sensitive imaging of functional groups in aqueous solutions by chemical force microscopy. *J. Am. Chem. Soc.* **119**, 2006–2015 (1997).
11. Cui, Y.; Wei, Q. Q.; Park, H. K.; Lieber, C. M. Nanowire Nanosensors for Highly-Sensitive, Selective and Integrated Detection of Biological and Chemical Species. *Science* **293**, 1289–1292 (2001).
12. Penner, R. M. Chemical sensing with nanowires. *Annu. Rev. Anal. Chem.* **5**, 461–485 (2012).

13. Hwang, S.-W. *et al.* A Physically Transient Form of Silicon Electronics. *Science* **337**, 1640-1644 (2012).
14. Kang, S.-K. *et al.* Dissolution Behaviors and Applications of Silicon Oxides and Nitrides in Transient Electronics. *Adv. Func. Mater.* **24**, 4427-4434 (2014).
15. M. R. Bruchas *et al.*, Selective p38 $\alpha$  MAPK deletion in serotonergic neurons produces stress resilience in models of depression and addiction. *Neuron* **71**, 498-511 (2011).
16. Kim, T. I. *et al.* Injectable, Cellular-Scale Optoelectronics with Applications for Wireless Optogenetics. *Science* **240**, 211-216 (2013).
17. Gaber, N., Khalil, D. & Shaarawi, A. Fabrication of optical filters using multilayered porous silicon. in *Advanced Fabrication Technologies for Micro/Nano Optics and Photonics IV* 7927, 79270S–79270S–9 (2011).
18. Bosch, S., Ferré-Borrull, J., Leinfellner, N. & Canillas, A. Effective dielectric function of mixtures of three or more materials: a numerical procedure for computations. *Surf. Sci.* **453**, 9–17 (2000).
19. Schmid, P. E. Optical absorption in heavily doped silicon. *Phys. Rev. B* **23**, 5531–5536 (1981).
20. Barrett, E. P., Joyner, L. G. & Halenda, P. P. The Determination of Pore Volume and Area Distributions in Porous Substances. I. Computations from Nitrogen Isotherms. *J. Am. Chem. Soc.* **73**, 373–380 (1951).
21. Kang, S. K. *et al.* Biodegradable Thin Metal Foils and Spin-On Glass Materials for Transient Electronics, *Adv. Func. Mater.* **25**, 1789-1797 (2015).
22. Yin, Y. *et al.* Dissolvable Metals for Transient Electronics. *Adv. Func. Mater.* **24**, 645-658 (2014).

**Table S1. Hydrolysis mechanisms and dissolution rates of key materials in this study (ACSF and PBS measured at 37 °C, DI at room temperature).**

Materials	Dissolution rate (nm/day)			Hydrolysis mechanism
	ACSF	PBS <sup>12,21</sup>	DI <sup>22</sup>	
Si NM	$2.3 \times 10^1$	$0.5 \times 10^1$		$\text{Si} + 4\text{H}_2\text{O} \rightarrow \text{Si}(\text{OH})_4 + 2\text{H}_2$
np-Si	$9.0 \times 10^3$	-	-	
SiO <sub>2</sub>	$0.8 \times 10^1$	$1.4 \times 10^1$		$\text{SiO}_2 + 2\text{H}_2\text{O} \rightarrow \text{Si}(\text{OH})_4$
Mg	$4.0 \times 10^3$	-	$1.7 \times 10^3$	$\text{MgO} + \text{H}_2\text{O} \rightarrow \text{Mg}(\text{OH})_2$
Mo	-	$2.0 \times 10^1$	$0.7 \times 10^1$	$2\text{Mo} + 2\text{H}_2\text{O} + 3\text{O}_2 \rightarrow 2\text{H}_2\text{MoO}_4$

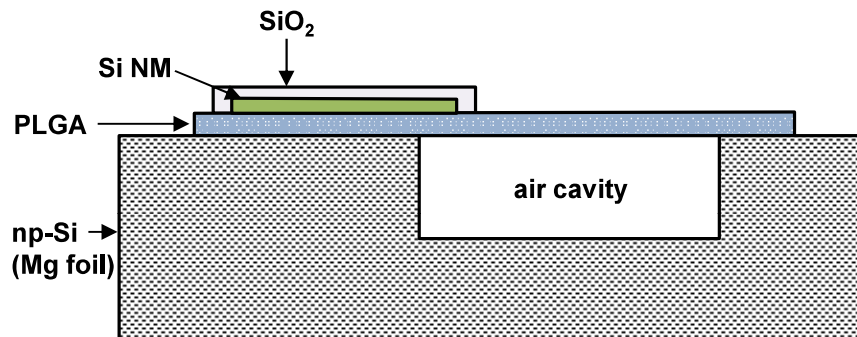


**Figure S1.** Cross-sectional side view of the bioresorbable pressure sensor.

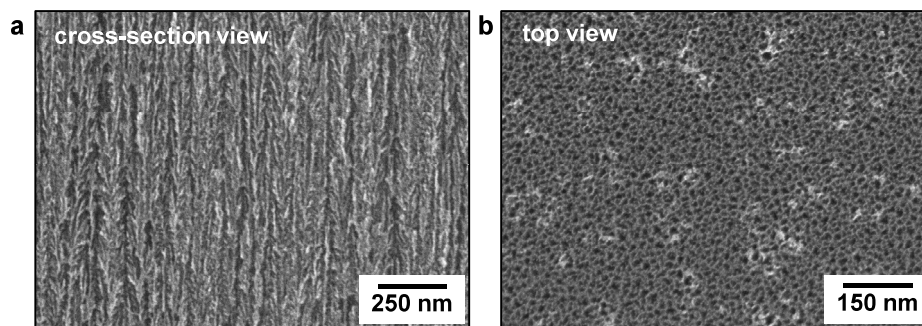


**Figure S2. Scanning electron microscope (SEM) images of nanoporous Si.** a) Cross-section view and b) top view of np-Si structure with ~71 % porosity.

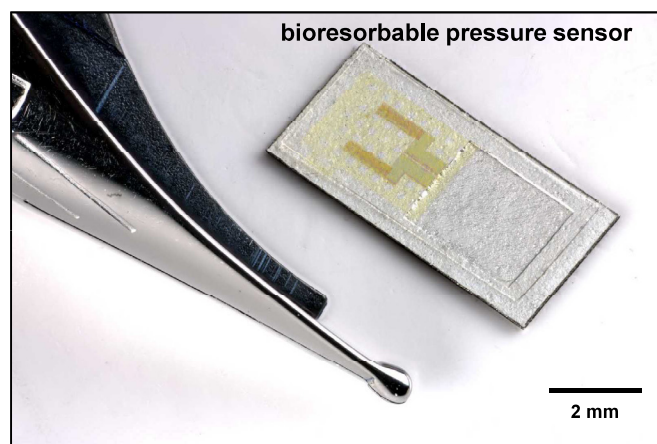


**Figure S3.** Biodegradable pressure sensor with Mg trench structure. Trench depth and thickness of Mg foil are  $\sim 40 \mu\text{m}$  and  $\sim 80 \mu\text{m}$ , respectively.

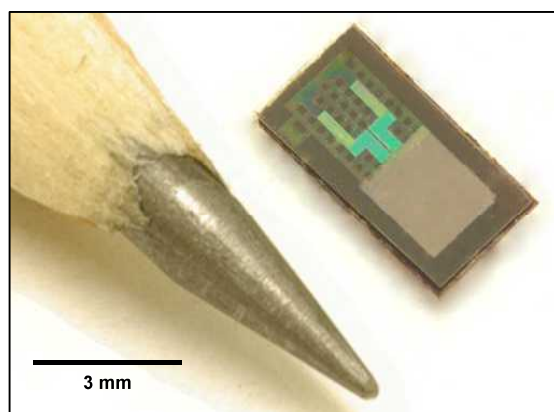
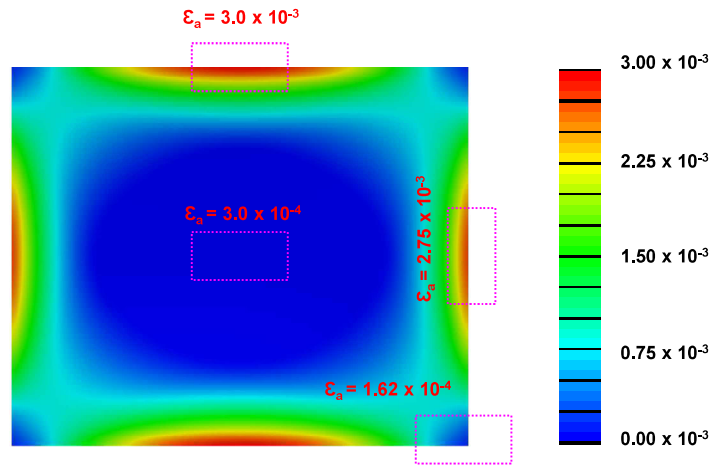


**Figure S4.** Image of a bioresorbable pressure sensor, with a thickness of  $\sim 110 \mu\text{m}$ , a weight of  $\sim 1 \text{ mg}$  and overall lateral dimensions of  $3 \text{ mm} \times 6 \text{ mm}$  and trench dimensions of  $2 \text{ mm} \times 2.4 \text{ mm} \times 40 \mu\text{m}$ .



max principal strain on top surface at 70 mmHg

Figure S5. Optimization of the location of the piezoresistive serpentine sensors.

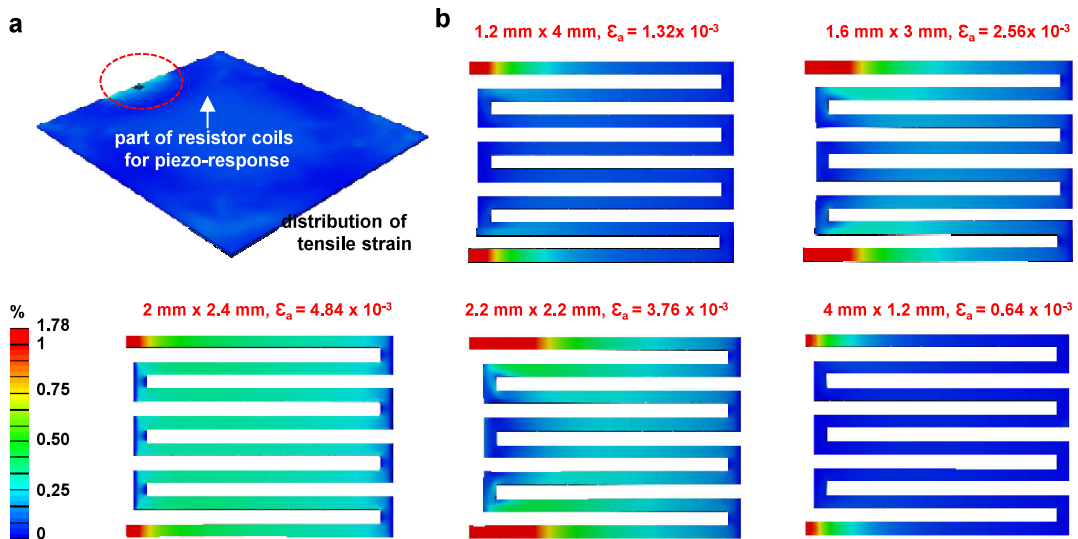
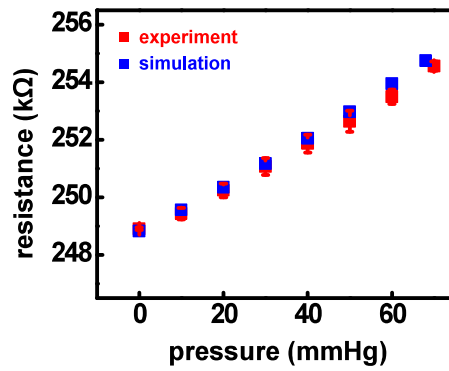
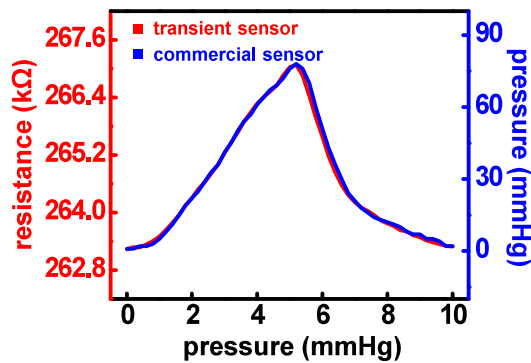


Figure S6. Optimization of trench geometry through stress-strain analysis using the finite element method (FEM). a) Full image of simulated dimension. b) Principle strain distribution around the piezoresistive serpentine sensors for various trench geometries.  $\epsilon_a$  represents average strain on coils.



**Figure S7.** Piezoresistive response of the pressure sensor compared to finite element method (FEM) simulation (error bars represents standard deviations).



**Figure S8.** Calibration curve of pressure sensor with 2 mm × 2.4 mm × 40 μm dimension.

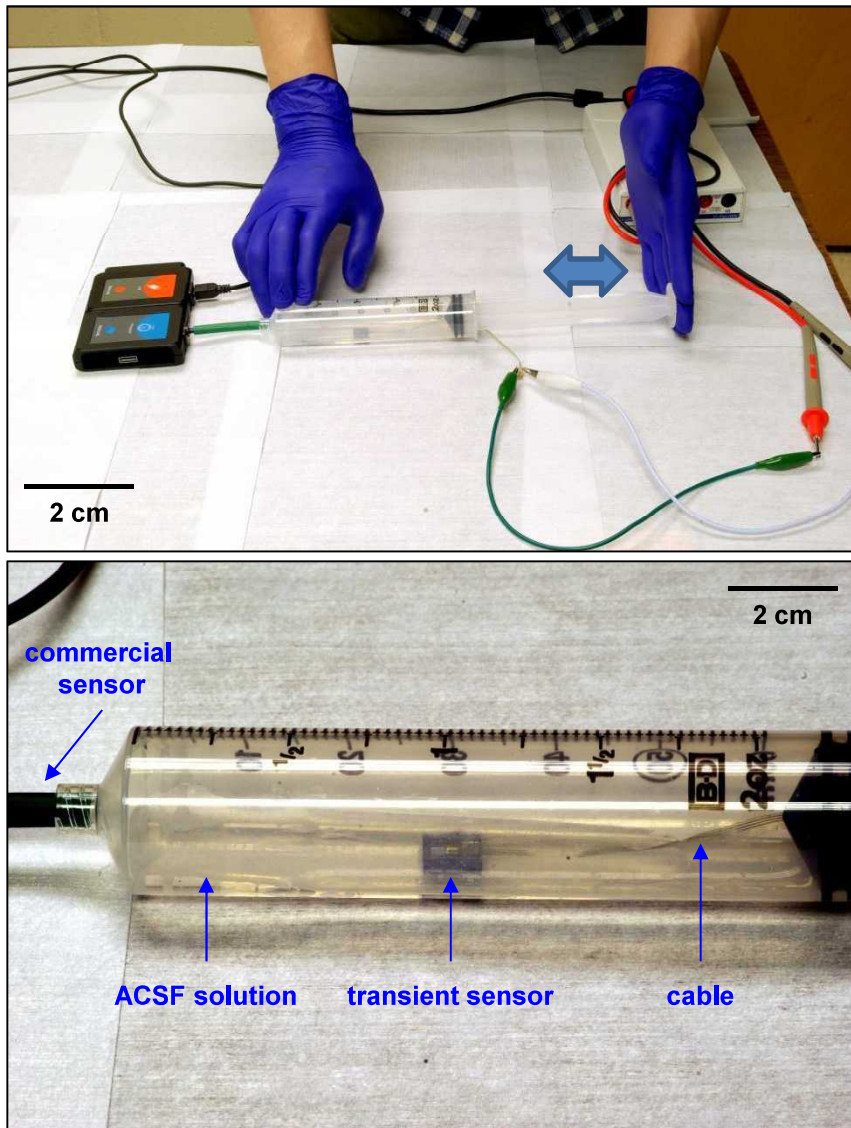


**Figure S9.** In vitro test of transient pressure sensor in ACSF solution.

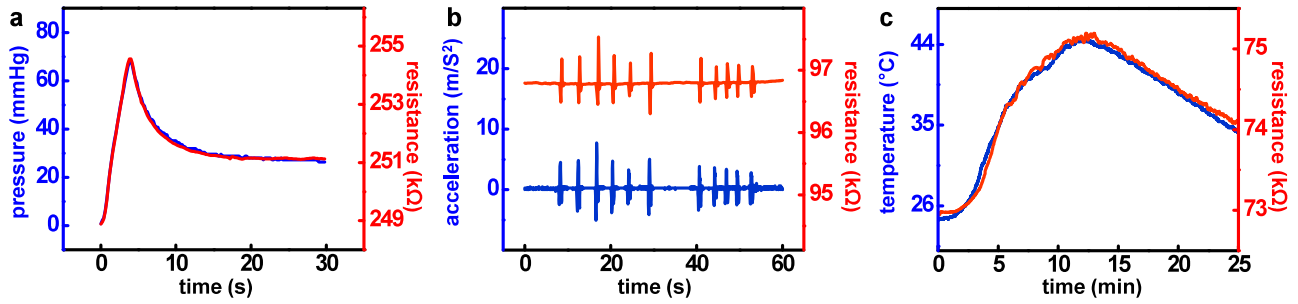


**Figure S10.** Calibration of resistance change to a) pressure, b) acceleration, and c) temperature.

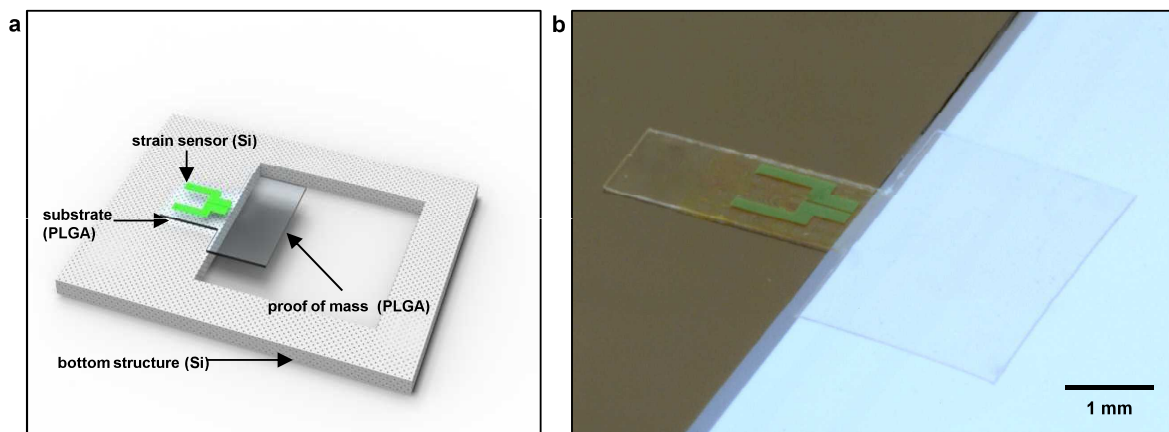


**Figure S11.** Transient accelerometer with Si-NM piezoresistive strain sensor. a) Materials and structure of accelerometer with PLGA proof mass. b) Image of bioresorbable accelerometer on the Si structure.

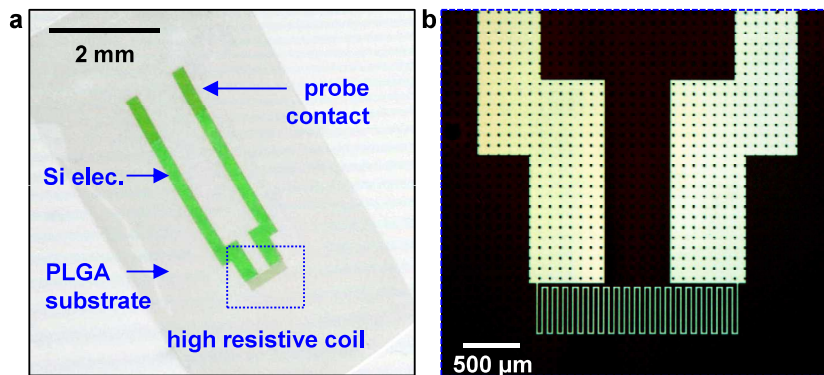


**Figure S12.** Bioresorbable temperature sensor on a thin PLGA film. a) Materials and structure of a thermoresistive Si temperature sensor. b) Microscope image of a dense serpentine Si-NM structure for enhanced thermoresistive response.

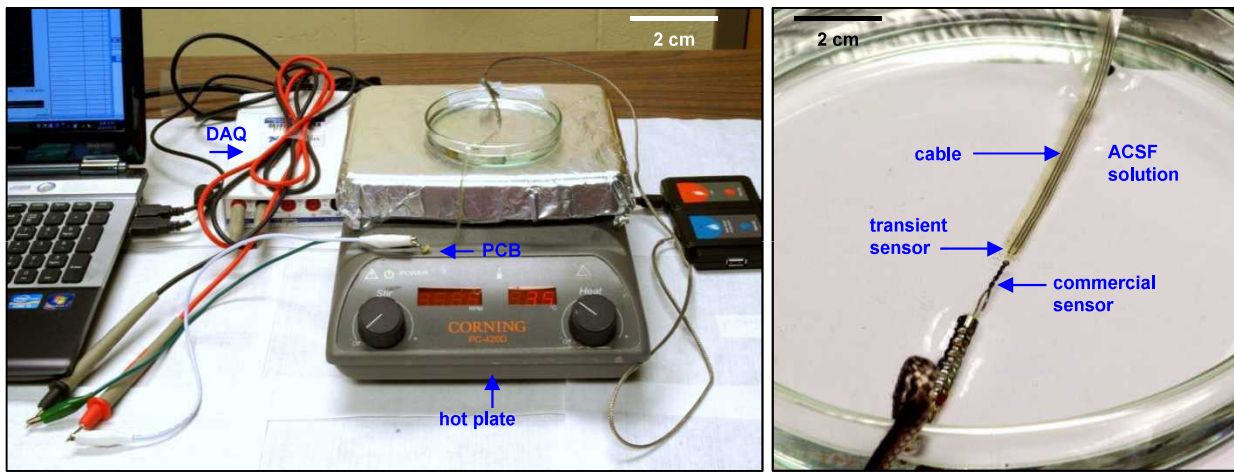


**Figure S13.** In vitro setup for transient temperature sensors.

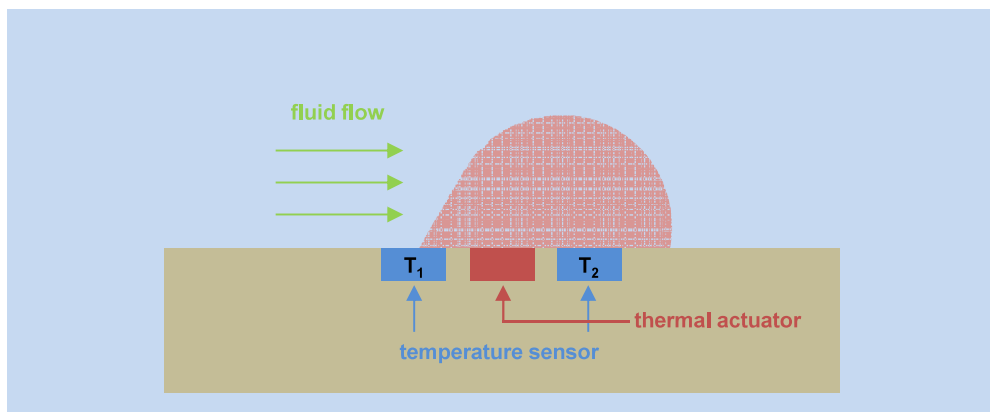


**Figure S14.** Principle of flow rate monitor based on a thermal actuator and a pair of temperature sensors. The difference between the temperatures recorded at the two temperature sensors ( $T_2 - T_1$ ) increases as the flow rate increase.

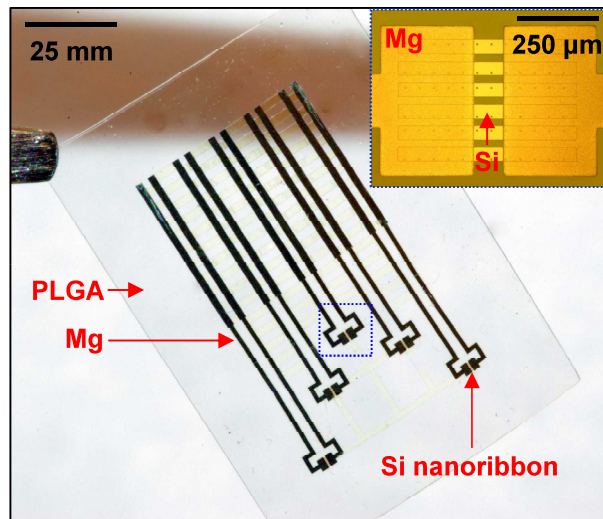


**Figure S15.** Bioresorbable pH sensor constructed with Si-NRs, Mg electrodes and PLGA substrates.

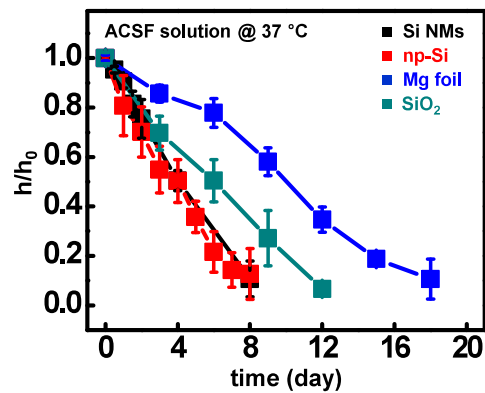


**Figure S16.** Hydrolysis kinetics of materials used in the bioresorbable pressure sensors. Normalized thickness ( $h/h_0$ ) as a function of time during dissolution of individual materials in artificial cerebrospinal fluid (ACSF) at physiological temperature (37 °C). The initial thicknesses were 200 nm for Si nanomembranes (Si NMs), 80 μm for porous Si (p-Si), 80 μm for Mg foil, and 100 nm for SiO<sub>2</sub>.

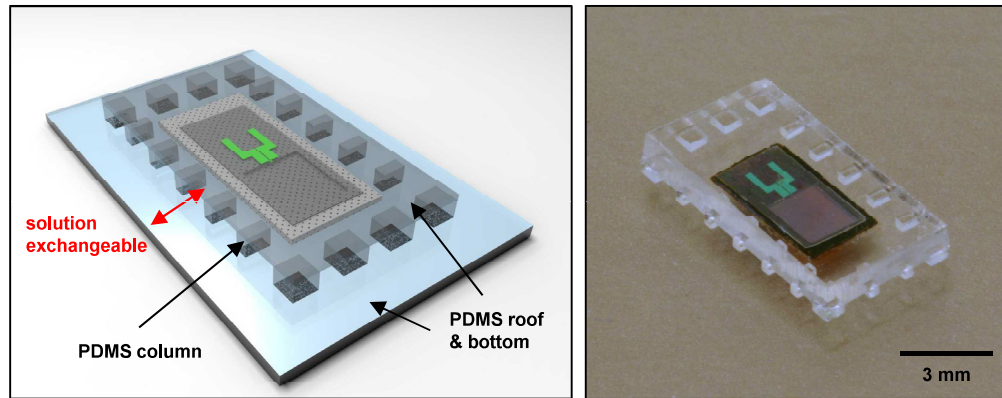


**Figure S17.** Schematic diagram (left) and image (right) of PDMS structure used as a simple mimic of the intracranial space.

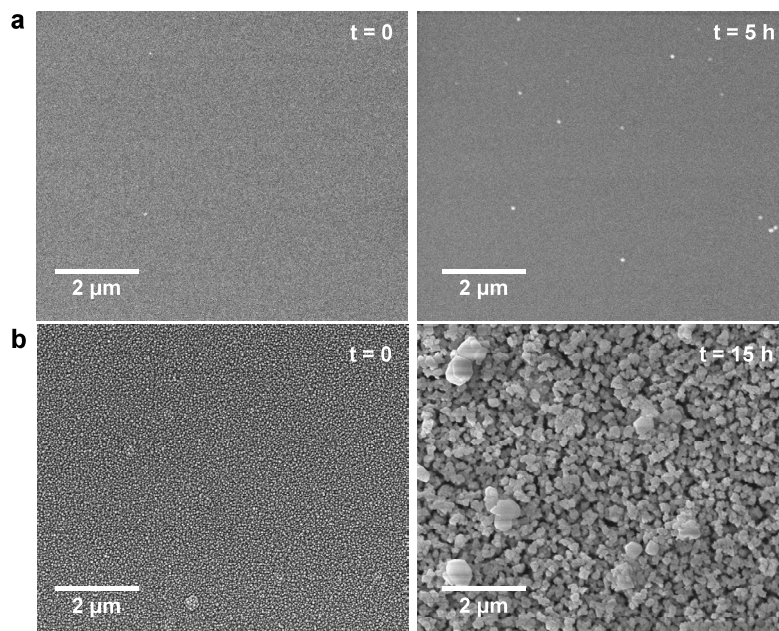


**Figure S18.** Scanning electron microscope (SEM) images of a) Si NMs and b) np-Si at the different stages of dissolution in buffer solution with pH 12 at 37 °C.

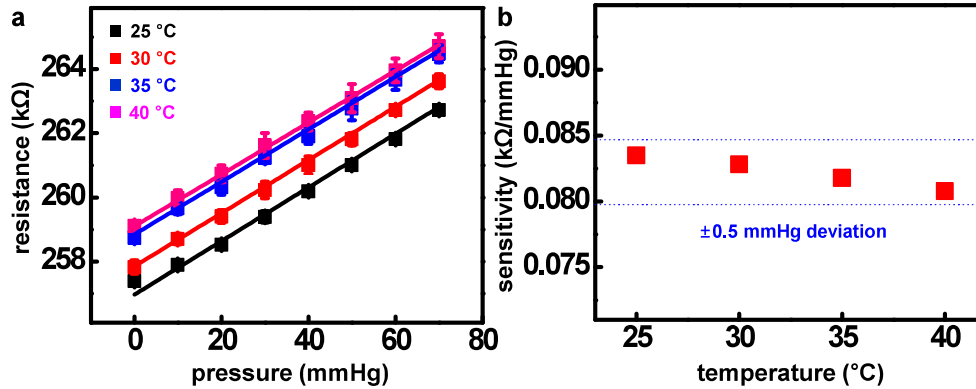


**Figure S19.** Calibration of the temperature dependent piezoresistivity. a) Resistivity variation to applied pressure at various temperatures (error bars represents standard deviation). b) Variation of sensitivity of resistivity to pressure associated with changes in temperatures. The change of piezoresistivity sensitivity is negligible across the expected range of brain temperatures.

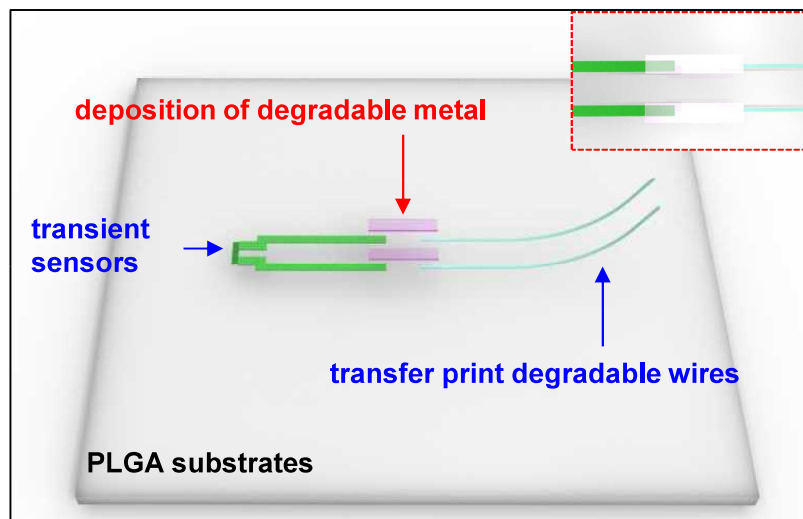


**Figure S20.** Strategy for interconnection between a bioresorbable device and degradable external wires on biodegradable polymer. Transfer printing the biodegradable wires (Mg or Mo) on the biodegradable polymer substrate (PLGA), and depositing dissolvable metal (Mo) between the wires and sensors yield the fully bioresorbable interface.

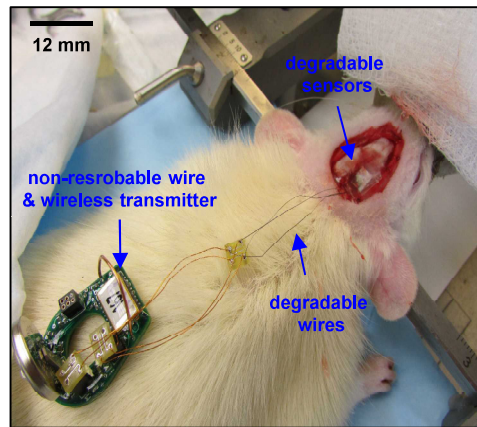


**Figure S21.** Image of the interface between the bioresorbable wires and the wireless transmitter.

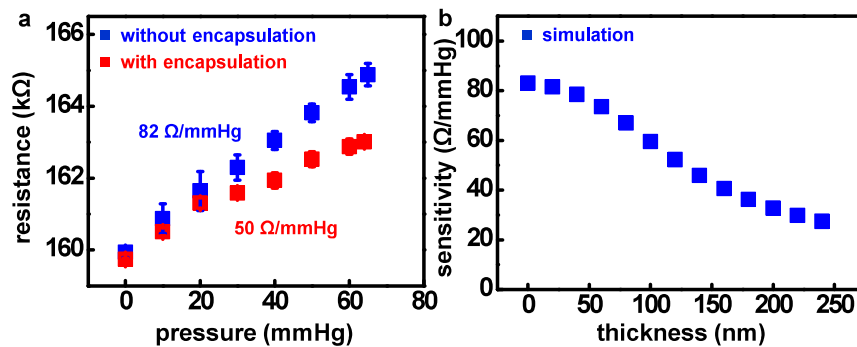


**Figure S22.** Effect of polyanhydride encapsulation on the response of the pressure sensor. a) Calibration curves before and after encapsulation. The calibration factor changes from 82 to 50  $\Omega/\text{mmHg}$  with 120  $\mu\text{m}$  thick encapsulation (error bars represents standard deviation). b) The thickness dependent sensitivity simulated by FEM.

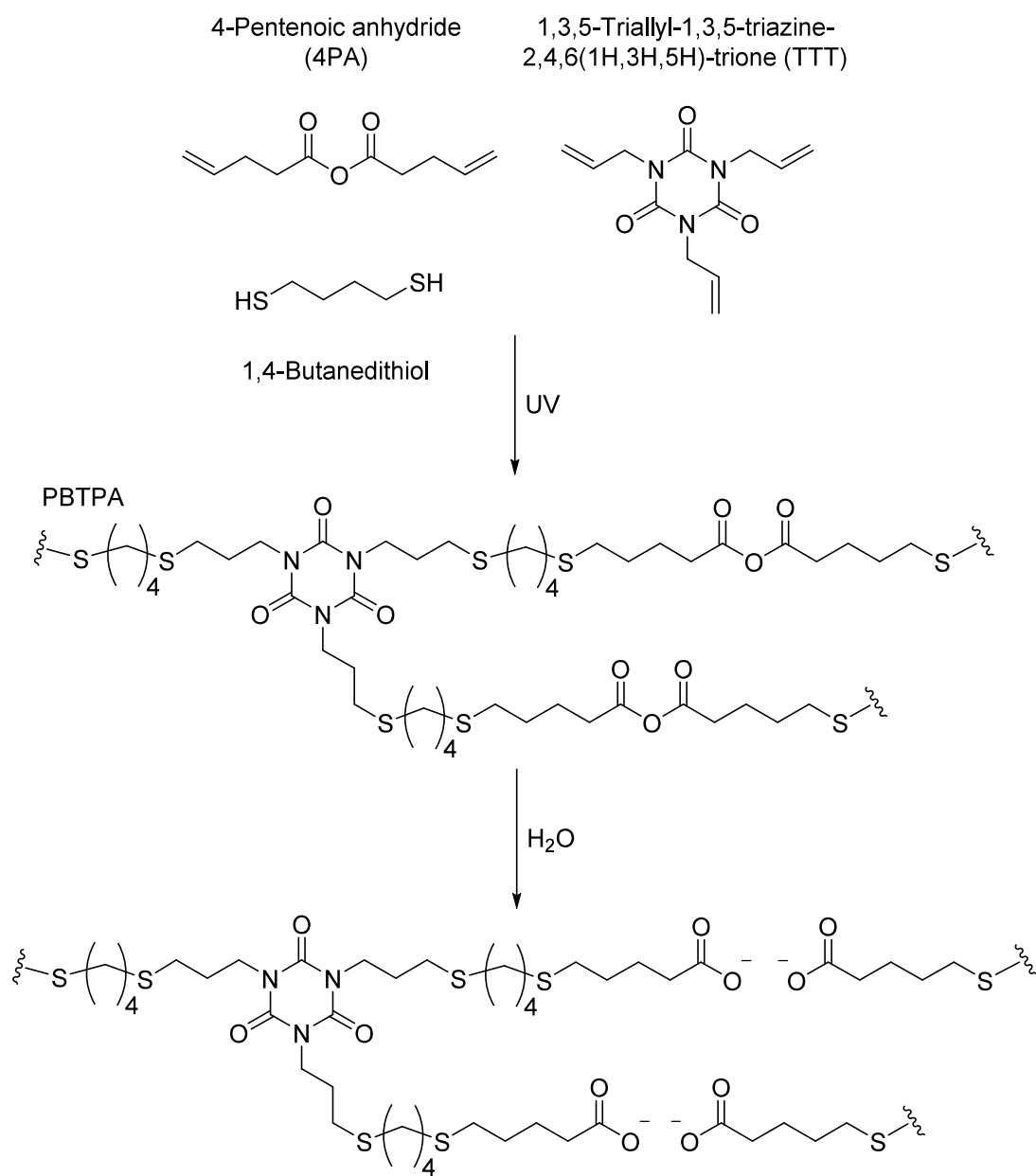


**Figure S23.** Chemistry of synthesis and hydrolysis of a biodegradable polymer (class of polyanhydride) for encapsulation.

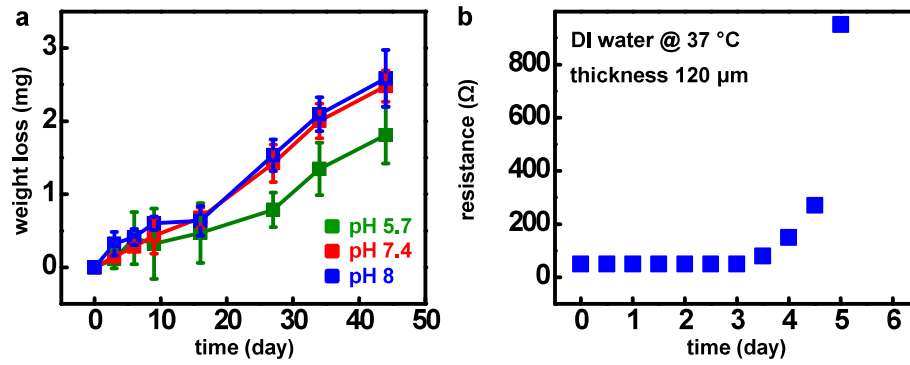


**Figure S24.** a) Dissolution kinetics and b) water permeability (tested by 300 nm thick Mg resistor) of polyanhydride encapsulation.

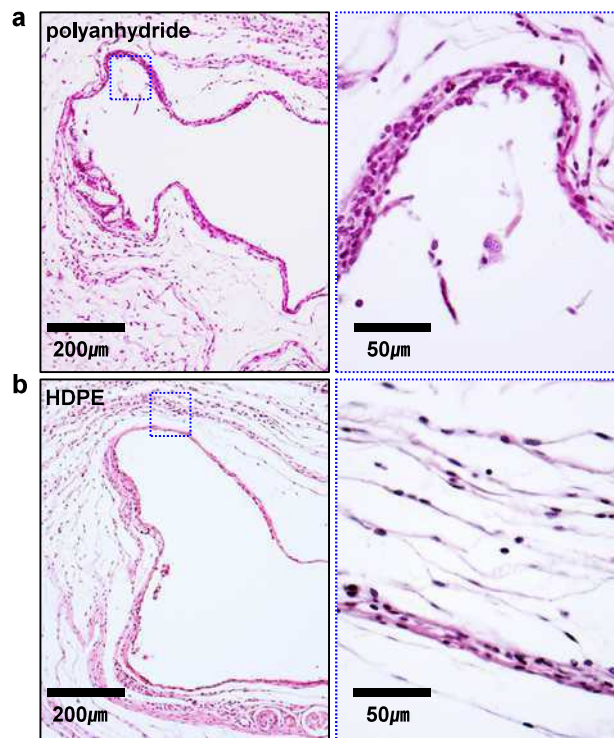


**Figure S25.** Hematoxylin and eosin (H&E) images of tissue around the implant site of a) polyanhydride and b) HDPE after 14 days.

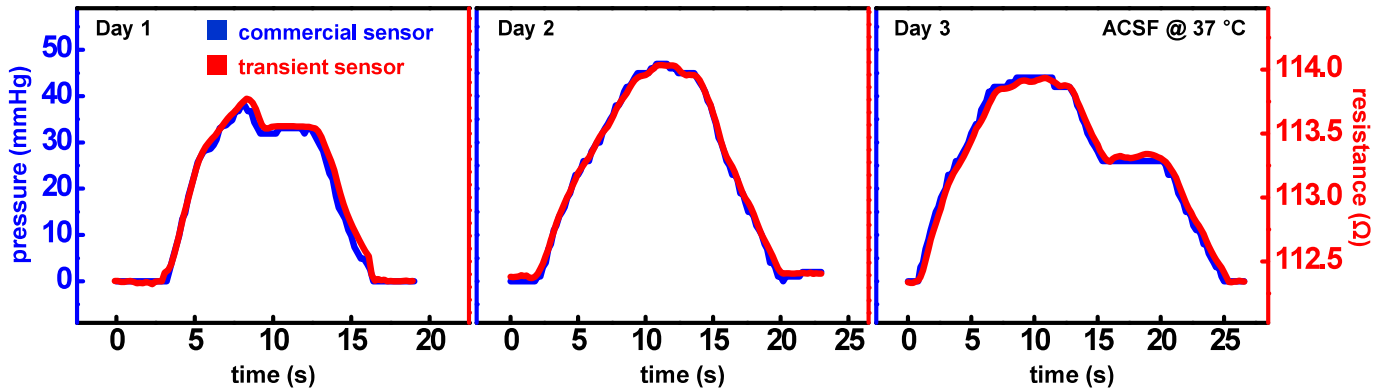


**Figure S26.** In vitro operation of bioresorbable pressure sensor with functional lifetime controlled with a biodegradable encapsulation layer.

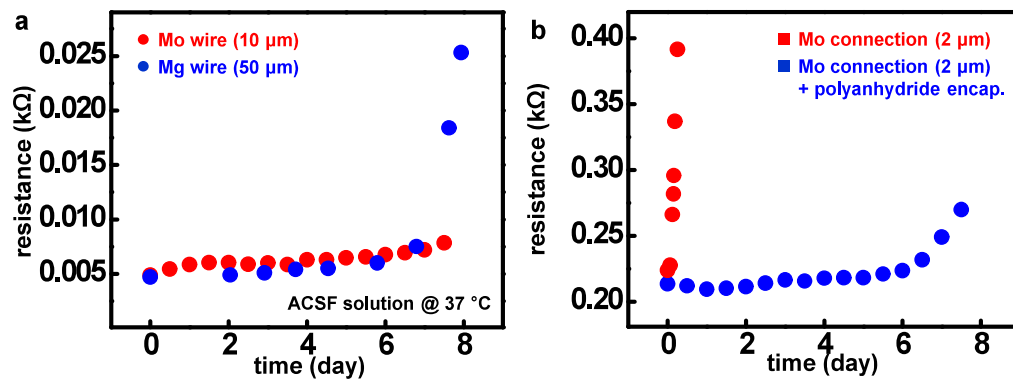


**Figure S27.** Effect of dissolution of metal wires and interconnects on the resistance.

a) Increases in resistance of biodegradable metal wire (Mo, 10 μm; Mg, 50 μm) in ACSF at physiological temperature for ~a week. The change in resistance is negligible (below a few ohms) for a week. The resistance of Mg wire rapidly increases after 7 days due to its higher dissolution rate compared to Mo. b) Changes in resistance of Mo interconnections (~ 2 μm) during hydrolysis in ACSF at body temperature.

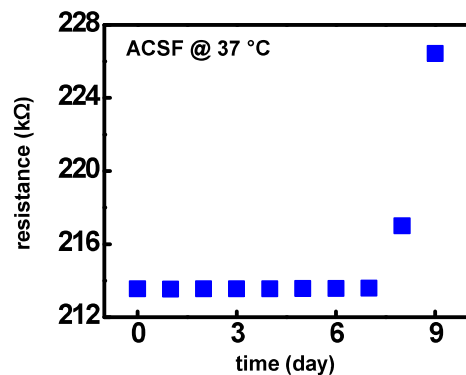


**Figure S28.** Resistance measurement of a pressure sensor with polyanhydride encapsulation with constant external pressure.

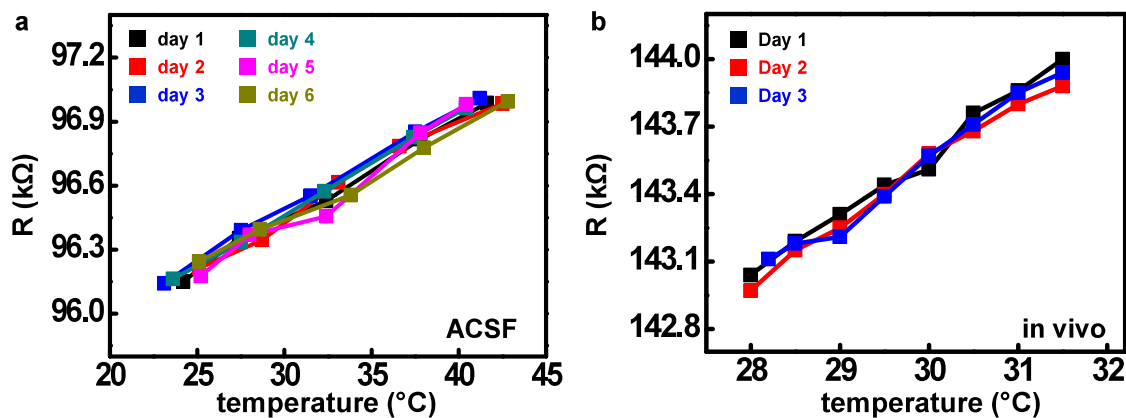


**Figure S29. In vitro and in vivo demonstrations of biodegradable temperature sensors.** a) Calibration curves for resistance to temperature indicate stable operation over 6 days in ACSF. b) Stable in vivo operation was demonstrated for three days. Sensors were encapsulated with a 120  $\mu\text{m}$  thick layer of polyanhydride.

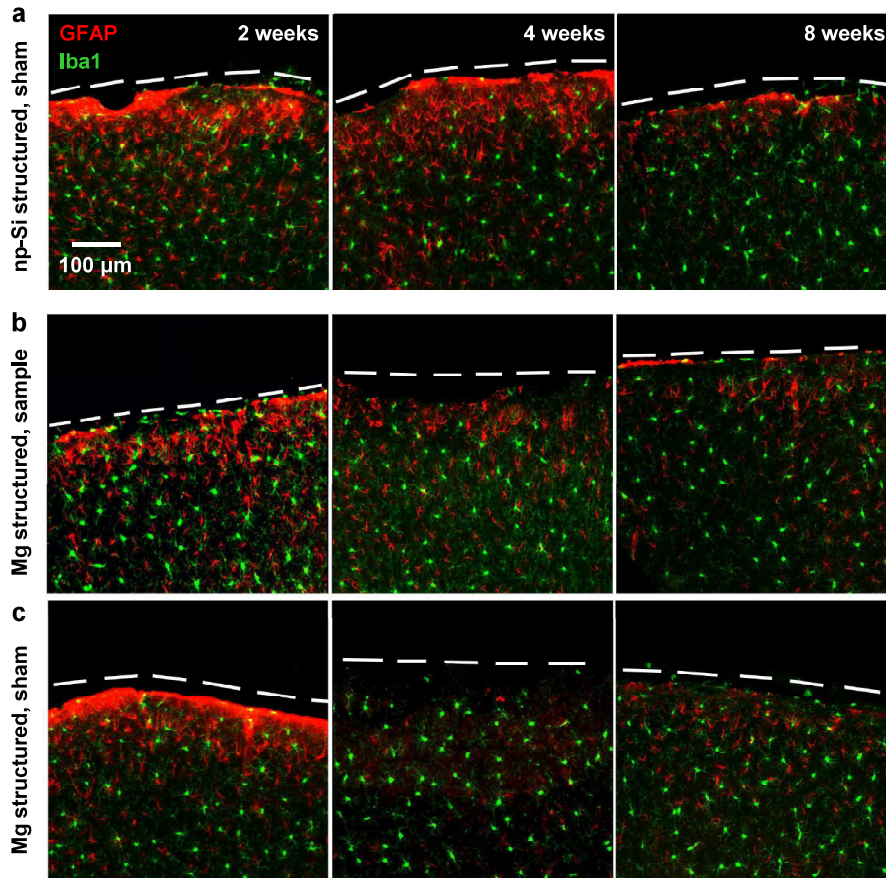


**Figure S30. Confocal fluorescence images of the cortical surface.** a) Series of images of the sham area (left side of brain) and the area underneath the np-Si pressure sensor (right side of brain). b) Image of the cortical surface at the site implanted with a Mg supported device and c) at the sham site.

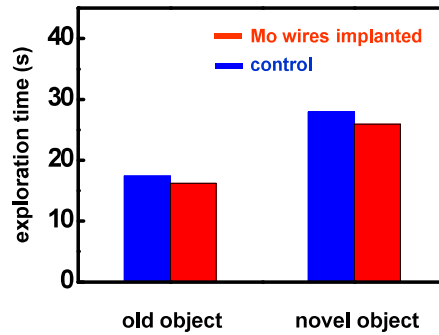


**Figure S31.** Animal behavior evaluation with transcutaneous wire implantation using novel object recognition test.

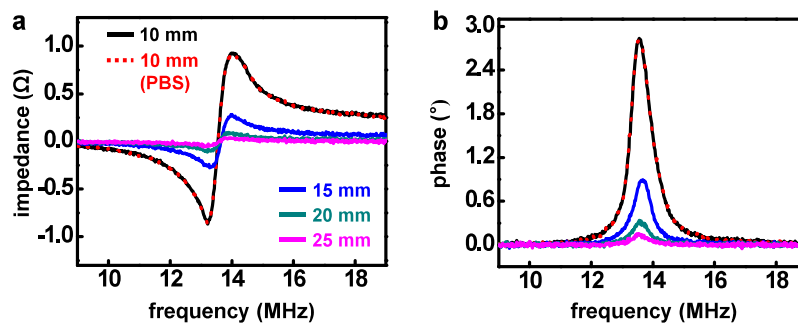


**Figure S32.** Frequency dependent a) impedance and b) phase of the NFC system at the different distance (black line; 10 mm, red dot; 10 mm with 2 mm barrier of phosphate buffer solution (PBS), blue line; 15 mm, cyan line; 20 mm, magenta line; 25 mm).

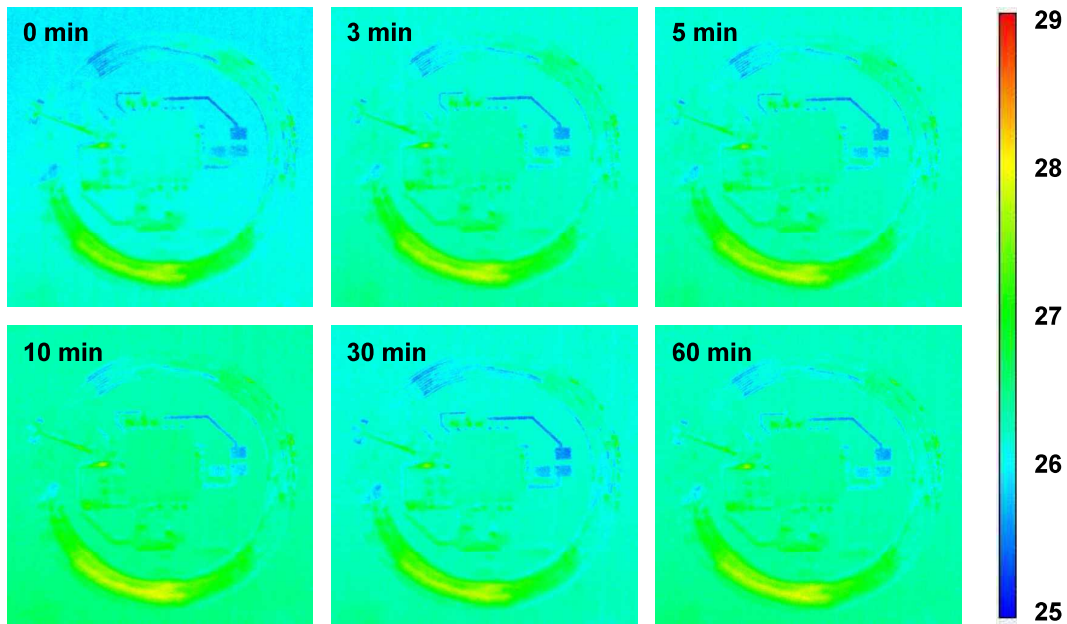


**Figure S33.** IR thermography of an NFC system during wireless operation in air.

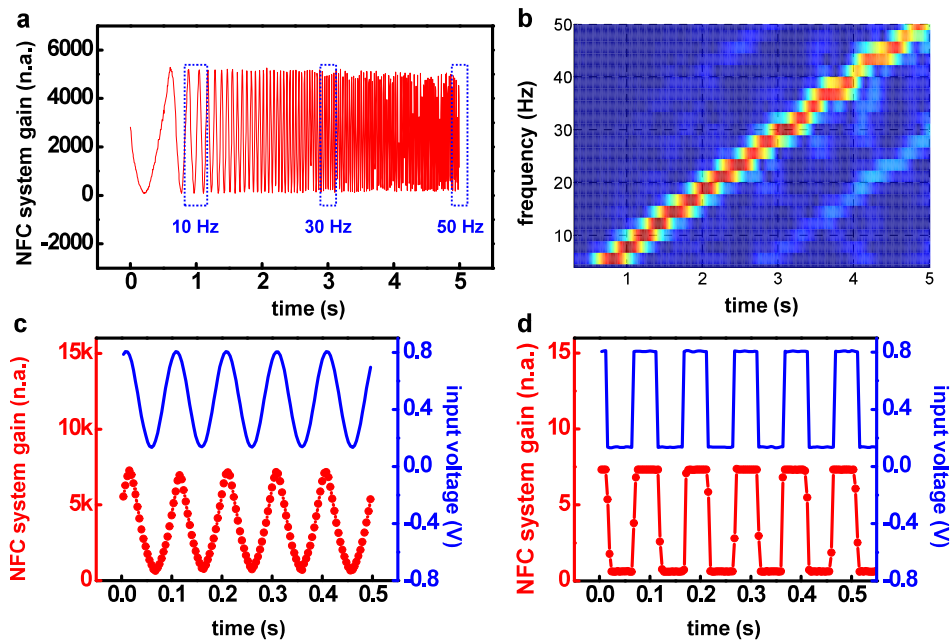


**Figure S34. High sampling rate of NFC system.** a) Wirelessly transmitted voltage sine waves with frequencies between 1 to 50 Hz. Maximum sampling rate of this system is 250 Hz. b) Spectrogram of swept sine wave in Figure 2f. High speed data acquisition of NFC system demonstrated with c) sine and d) square wave of 10 Hz frequency. (Red dot line is the data point measured by NFC system and blue line is input signal from signal generator.)

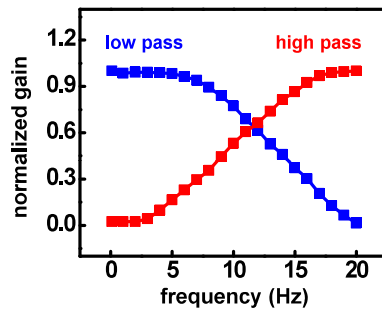


**Figure S35.** Gain response of programmed real-time high (red) and low (blue) pass filtering, performed by the NFC chip, as a function of frequency.

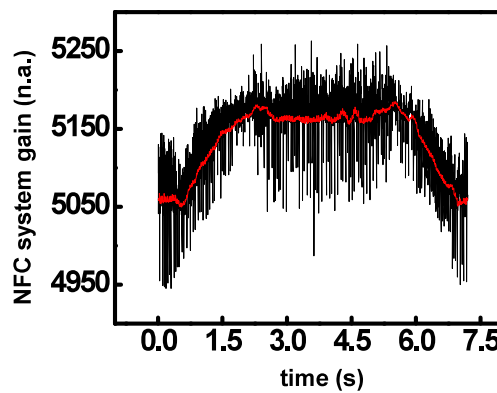


**Figure S36.** Comparison of filtered (red) and unfiltered (black) gain during pressure measurement. Two channels were measurement through NFC system at the same time. The filter function was loaded and performed in the chip.

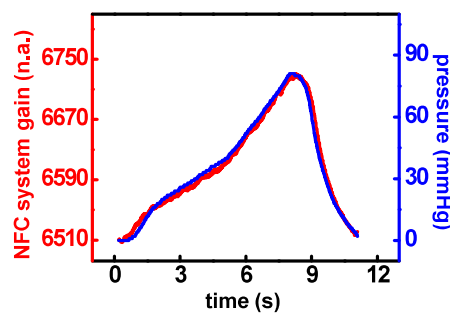


**Figure S37.** Response of a commercial pressure sensor (blue) and a wireless, biodegradable system (red) to time-varying pressure over a range relevant to intracranial monitoring.

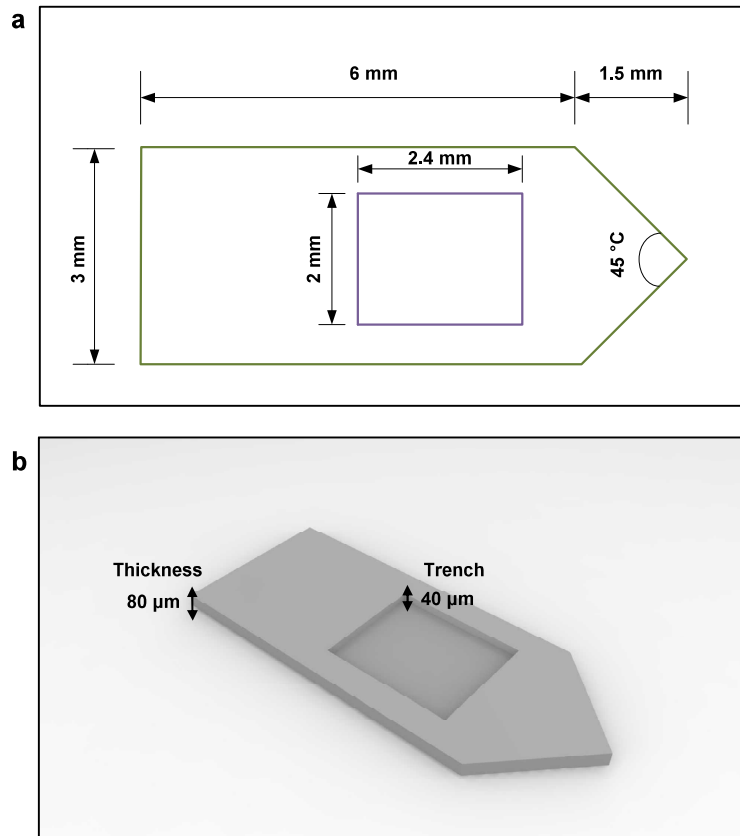


**Figure S38. Geometry of needle substrates of pressure sensor.** a) Lateral geometry and b) three dimensional geometry of Mg needle substrates.

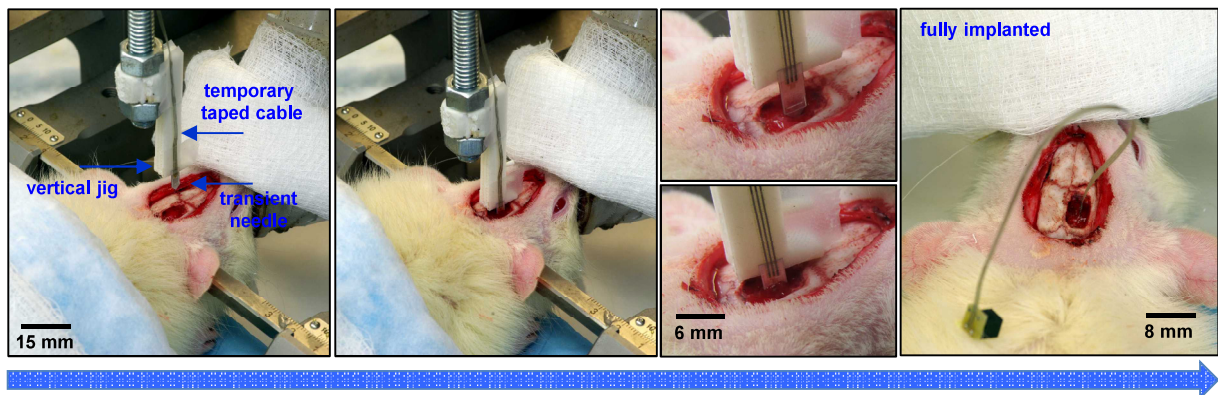


**Figure S39. Surgical process for injectable form of biodegradable sensors.** A needle shaped sensor was positioned with a jig. Lowering the jig causes the sharp edge of the device to penetrate into the deep brain.